Chemical Geology 708 (2026) 123332

Contents lists available at ScienceDirect

Chemical Geology

journal homepage: www.elsevier.com/locate/chemgeo

Redistribution of uranium and co-occurring metals from mining-inherited deposits recorded in a wetland

Louise Darricau [a,b,*], Alexandra Courtin [b], Josselin Gorny [a], Alkiviadis Gourgiotis [a], David Suhard [a], Emmanuel Joussein [c], Solenn Réguer [d], Sebastian Schöder [d], Julia Cucinotta [a], Pascale Blanchart [a], Mathilde Zebracki [a], Arnaud Mangeret [a,**]

[a] Autorité de sûreté nucléaire et de radioprotection (ASNR), PSE-ENV/SPDR/LT2S, PSE-ENV/SERPEN/BERAD, PSE-SANTE/SESANE/LRSI, F-92260 Fontenay-aux-Roses, France
[b] Université Paris-Saclay, CNRS, GEOPS, 91405 Orsay, France
[c] Université de Limoges, E2Lim, 87000 Limoges, France
[d] Synchrotron SOLEIL, 91190 Saint Aubin, France

ARTICLE INFO

Editor: Dr. Karen Johannesson

Keywords:
Wetland contamination
Mining influence
Solid speciation
Uranium
Metals

ABSTRACT

The legacy of former uranium (U) mining activities led to the dispersion of inherited materials enriched with U-series nuclides and metal-rich minerals. In this study, the fate of U and associated metals *i.e.*, copper (Cu) and lead (Pb) in a wetland located downstream of a former U mining site was evaluated. This assessment was conducted through the identification of U sources in wetland soils, the solid speciation of U and co-occurring metals, and their reactivity under oxidizing conditions.

Our results confirmed that the mining materials in the wetland originated from the physical and chemical treatments of two U ores (Bois-Noirs-Limouzat (BNL) and Rophin). The investigation of solid metal-bearing species revealed that, in the pure BNL-inherited layer, U, Cu, and Pb species were associated to amorphous and crystalline Fe oxyhydroxides and clay minerals and to a lesser extent, in the form of U oxides and chalcopyrite. For the Rophin-originated deposits, the absence of crystalline U-inherited minerals was highlighted, with a significant association of U and Pb with organic matter, Fe-bearing species, and/or the clay mineral fraction. These results suggested redistribution from primary to secondary phases during alteration and pedogenesis processes. Deionized water-normalized leaching tests indicated different mass amounts mobilized from the two types of U-mining materials identified. These differences could be attributed to i) the occurrence of redox-sensitive minerals and ii) the presence of organic matter, which led to the formation of secondary higher stable metal species. This study provided new insights into the post-depositional transformation of mining-derived materials and the need to consider the mineralogy of parent materials.

1. Introduction

The legacy of U mining activities led to the production of mill tailings and waste rock, which resulted in the dispersion of co-occurring metals and radionuclides in the surrounding environments, including wetlands (Cuvier et al., 2016; Wang et al., 2013, 2014; Stetten et al., 2018b, 2020; Martin et al., 2020).

Recent studies led to a better knowledge regarding U redistribution mechanisms in environments submitted to water table fluctuations. It was notably found that reduced U-rich minerals such as U phosphate minerals (*e.g.* ningyoite $(U,Ca,Ce)_2(PO_4)_2 \bullet 1\text{-}2(H_2O)$), were prone to oxidative dissolution and formation of U(VI) complexed to particulate organic matter (POM), followed by subsequent reduction into U(IV) organic complexes (Stetten et al., 2018a, 2020). However, these mechanisms did not reveal significant U releases of soil-bound U to surface waters (Gilson et al., 2015) and that U remobilization from U(IV) phosphate minerals was intricately linked to U(VI) adsorption on the soil matrix (Stetten et al., 2020). Studies on U speciation in sediments,

* Corresponding author at: Autorité de sûreté nucléaire et de radioprotection (ASNR), PSE-ENV/SPDR/LT2S, PSE-ENV/SERPEN/BERAD, PSE-SANTE/SESANE/LRSI, F-92260 Fontenay-aux-Roses, France.
** Corresponding author.
E-mail addresses: louise.darricau@asnr.fr (L. Darricau), arnaud.mangeret@asnr.fr (A. Mangeret).

https://doi.org/10.1016/j.chemgeo.2026.123332
Received 21 November 2025; Received in revised form 20 February 2026; Accepted 25 February 2026
Available online 26 February 2026

wetlands and floodplains have shown that U is mainly present as mononuclear complexes of U(VI), predominantly, or U(VI), depending on the redox conditions. U was found associated with C-, P-, or Si- and its adsorption onto the POM, particularly *via* carboxyl function groups, plays a key role in controlling its mobility (Cumberland et al., 2018; Lefebvre et al., 2022; Mikutta et al., 2016; Noël et al., 2017; Regenspurg et al., 2010; Stetten et al., 2018b; Wang et al., 2014). The mobility and fate of U in natural and mining-impacted wetlands are thus strongly influenced by its interactions with reactive mineral phases, particularly iron minerals, clays, and natural POM. Fe(III) oxyhydroxides act both as major sorbents for U(VI) and as redox-active phases capable of mediating U(VI) reduction to less soluble U(IV), either biologically through microbial activity or abiotically *via* Fe^{2+} (Behrends and Van Cappellen, 2005; Fredrickson et al., 2000; Liger et al., 1999; Sani et al., 2004; Veeramani et al., 2011; Wang et al., 2014). Clay minerals containing structural Fe(III), as well as redox-reactive Fe-bearing minerals such as hematite, green rust, magnetite, and pyrite, strongly influence U behavior through adsorption, surface complexation, and redox transformations, thereby controlling both U speciation and mobility in these environments (Aamrani et al., 2007; Behrends and Van Cappellen, 2005; Fredrickson et al., 2000; Liger et al., 1999). Field studies in mining-impacted wetlands have shown that non-crystalline U(IV) has been observed bound to Fe- and organic-rich colloids that may include clay-associated material and be mobilized into porewater and surface water, challenging the assumption that reduced U is immobile under anoxic conditions (Wang et al., 2013). Despite significant advances in the knowledge of mechanisms controlling U fate in wetland environments, few studies have addressed the behavior of co-occurring metals directly associated with U-rich mineral or metal-rich crystalline phases present in the original U ore bodies (Doughman et al., 2024; Lin et al., 2024).

Indeed, the ore extraction processes, as well as natural weathering and erosion of the extracted mining materials, could mobilize additional elements other than U, such as metals and metalloids, including arsenic (Chen et al., 2009), vanadium (Avasarala et al., 2017), nickel (Donahue et al., 2000) and molybdenum (Essilfie-Dughan et al., 2011). These elements must be considered when establishing contaminated site management strategies. For example, in the former U mine of South Terras (UK), the existence of U attenuation mechanisms was mainly due to the co-precipitation of a U-As-rich metazeunerite ($Cu(UO_2)_2(AsO_4)_2•8H_2O$) and Cu-U-rich metatorbernite ($Cu(UO_2)_2(PO_4)_2•8H_2O$) solid solution (Corkhill et al., 2017). Similarly, U- and V-rich mineral phases like carnotite ($K_2(UO_2)_2(VO_4)_2•3H_2O$) and As-Fe-rich bearing phases were identified to mainly control the availability of U, V and As from abandoned mine waste in a Native American Community in Arizona (USA) (Avasarala et al., 2017; Blake et al., 2015). In addition, the presence of metals could significantly modify the geochemical behavior of U minerals, as shown for other elemental associations in other mine tailings (Monneron-Gyurits et al., 2020), for example by increasing bioavailability and/or bioaccessibility. In France, U mining activities began in 1946, with particular emphasis on the exploitation of U-rich pitchblende (UO_2) veins. Furthermore, the western Lachaux U-ore bodies located in the French Massif Central were also studied because of the exceptional predominance of U- and Pb-rich phosphate minerals, with mainly parsonsite ($Pb_2(UO_2)(PO_4)_2•2H_2O$) and to a lesser extent torbernite ($Cu(UO_2)_2(PO_4)_2•12H_2O$) and autunite ($Ca(UO_2)_2(PO_4)_2•10–12H_2O$) (Geffroy and Sarcia, 1955). A previous study demonstrated the accumulation of U and its daughter isotopes (^{226}Ra and ^{210}Pb) in a wetland located downstream the former U mining sites of the Lachaux district (Rophin). It suggested that this U record was related to the discharge of U-rich particles during the operations of U-ore processing plant (Martin et al., 2020). Also, the isotope tracing study of Geng et al. (2024) demonstrated that distinct mining-impacted layers could be identified within the same wetland soil core. These differences were the result of the physical and chemical processing of two types of U-ores, including U-phosphate species from Rophin deposits and pitchblende from the BNL deposits. Additionally, these two ores differ in mineralogical composition and associated trace metal inventory. While Rophin ores contain a high proportion of secondary U-bearing phases and Pb-phosphate minerals (parsonsite $Pb_2(UO_2)(PO_4)_2•2H_2O$, pyromorphite $Pb_5(PO_4)_3Cl$), BNL ore is characterized by sulfide-rich assemblages with presence of pyrite (FeS_2), marcassite (FeS_2) and chalcopyrite ($CuFeS_2$) (Cuney, 1978; Chautard et al., 2020). The presence of co-occurring metals in U-rich phosphate minerals, such as Pb and Cu, and accessory metal-bearing phases in U-mining waste, including metal-rich sulfide species, requires the investigation of specific mechanisms affecting the mobility of Cu, Pb, and U from mining deposits in the wetland.

This knowledge is of particular significance in environmental systems, given that redox transitions in wetland soils are largely controlled by seasonal hydrological disturbances (Gu et al., 2012). During flood events, irrigation of wetland soils resulted in oxygen consumption and the generation of reducing conditions (Weber et al., 2009). In contrast, intense drought events cause air penetration to the pore space, which may result in the oxidative dissolution of metal-bearing sulfide precipitates, such as Zn (Bostick et al., 2001; Priadi et al., 2012) and Pb sulfides (Dewey et al., 2021). The effects of oxidation events on the reactivity of co-occurring metals in former secondary uranium mining deposits remain poorly understood.

The study aimed to understand the origin, solid speciation, and the reactivity of metal-bearing phases, particularly Cu, Pb and U, in a contaminated wetland soil influenced by U mining activities. Such knowledge is necessary to better anticipate the long-term behavior of metals in such environments. This wetland is characterized by seasonal water level fluctuations driven by precipitation and drainage conditions (Martin et al., 2020, 2021), leading to alternating oxic and suboxic to anoxic conditions in soil layers (Martin et al., 2021). Moreover, the contrasts between the two ores (BNL and Rophin) are expected to influence both the initial release of U during ore processing and its subsequent redistribution in downstream environments. This work was specifically focused on: i) the determination of the origin of U-rich species sequestrated in the wetland allowing to understand the associated metals contents, geochemical fate and behavior; ii) the identification of the metal host phases through the mineralogical assemblages; and iii) the evaluation of the reactivity of U and other metal-bearing phases under oxidizing conditions. To address these three objectives, the identification of the origin of U-rich species in mining materials was based on bulk and grain-scale stable Pb isotope analyses, respectively determined by ICP-MS/MS and Secondary Ion Mass Spectrometry (SIMS), allowing the discrimination of different processed U ore sources. In addition, the identification of U-bearing phases was performed with Scanning Electron Microscopy (SEM) equipped with an Energy-Dispersive X-Ray (EDX) probe, and Electron Probe Micro-Analysis (EPMA) for less U-enriched minerals. The identification of U, Cu, and Pb host phases in dried wetland soil core samples were assessed using selective and BCR-type sequential chemical extraction procedures combined with micro-X-Ray Absorption Near-Edge Structure spectroscopy (μXANES) and the abovementioned techniques. Despite technical limitations in terms of resolution or detection thresholds, their integration provided a coherent understanding of metal associations. Additionally, the evaluation of the easily extractable fraction of metals from U-mining deposits was performed according to a one-step deionized water leaching test. In this study, the term “available” was used to describe this fraction.

2. Material and methods

2.1. Site description

The study area is the watershed of the former Lachaux mining site (communes of Lachaux and Ris – Puy-de-Dôme), located in the Forez Massif, east of the Limagne Graben in the northeastern part of the Puy de

Dôme department in France (Fig. 1) (Guiolliard, 2002). Prospecting, exploitation, and physical processing of U ores occurred from 1947 to 1959 in several U mining sites: Rophin, Gagnol, Etang du Reliez, Reliez and Bancherelle (IRSN, 2024). The mineralogical assemblage of the ore was characterized by the abundance of smoky quartz with large sulfide crystals, *i.e.*, galena (PbS) and chalcopyrite ($CuFeS_2$), associated with rare pyrite (FeS_2) and sphalerite (ZnS).

U-rich minerals consisted of parsonsite ($Pb_2(UO_2)(PO_4)_2 \bullet 2H_2O$), autunite ($(Ca(UO_2)_2(PO_4)_2 \bullet 8\text{-}12H_2O)$) and torbernite ($Cu(UO_2)_2(PO_4)_2 \bullet 12H_2O$) (Geffroy and Sarcia, 1955). The ore washing plant built at the Rophin site in 1948 led to the extraction of 400 kg of U from the average ore concentration of 2‰. In 1957, chemical treatment tests were conducted for the pitchblende of the BNL U ore (Martin et al., 2020). After the closure of the mine, 30,000 tons of waste and U mill tailings were covered with vegetated soil and stored *in situ* under the regulations of the French Installation Classified for the Protection of the Environment (ICPE), and forest vegetation has developed. In the western part of this ICPE, a trench collects the aqueous effluents from the former underground works (Himeur and Andres, 2012). These effluents feed the Gourgeat stream which is connected to the other local ore bodies of the Lachaux area. During mining operations, the Gourgeat watershed was closed 2 km downstream by a dam, near the confluence between the Gourgeat and Terrasson streams for the water supply of the ore processing plant (Martin et al., 2020). Significant enrichments of ^{238}U and its daughter isotopes have been found in wetland soil samples, because of the historical discharge of U-mining effluent from the ore washing treatment plant. These radionuclides were predominantly retained beneath a surface layer rich in organic matter, which acted as a geochemical barrier and favored their accumulation over time (Martin et al., 2020).

2.2. Sampling and on-site measurement procedures

In April 2019, a 50 cm deep soil core named "ZH" was sampled in the Rophin wetland (46°00′25.2″N 3°33′00.3″E) using a Russian corer (Eijkelkamp). After sampling, the soil core was divided into 23 samples every 2–3 cm on site without preserving soil redox characteristics. This approach permits us to specifically investigate U and metal behavior under oxidizing conditions, which are relevant during low-water or post-disturbance periods. Consequently, the results reflect potential remobilization scenarios rather than strictly *in situ* speciation. Three main layers were distinguished and described in the Section 2.1: the horizon "ZH1" as an organic-rich surface layer (0–10 cm depth), the horizon "ZH2" (12–20 cm depth) defined as mining deposits inherited from the treatment of U ores described by Martin et al., 2020 (Fig. 1), and the horizon "ZH3" (22–50 cm depth) considered as the original soil (Martin et al., 2020). At 10–12 cm and 20–22 cm, these depths were considered as interface zones, potentially representing a mix of the

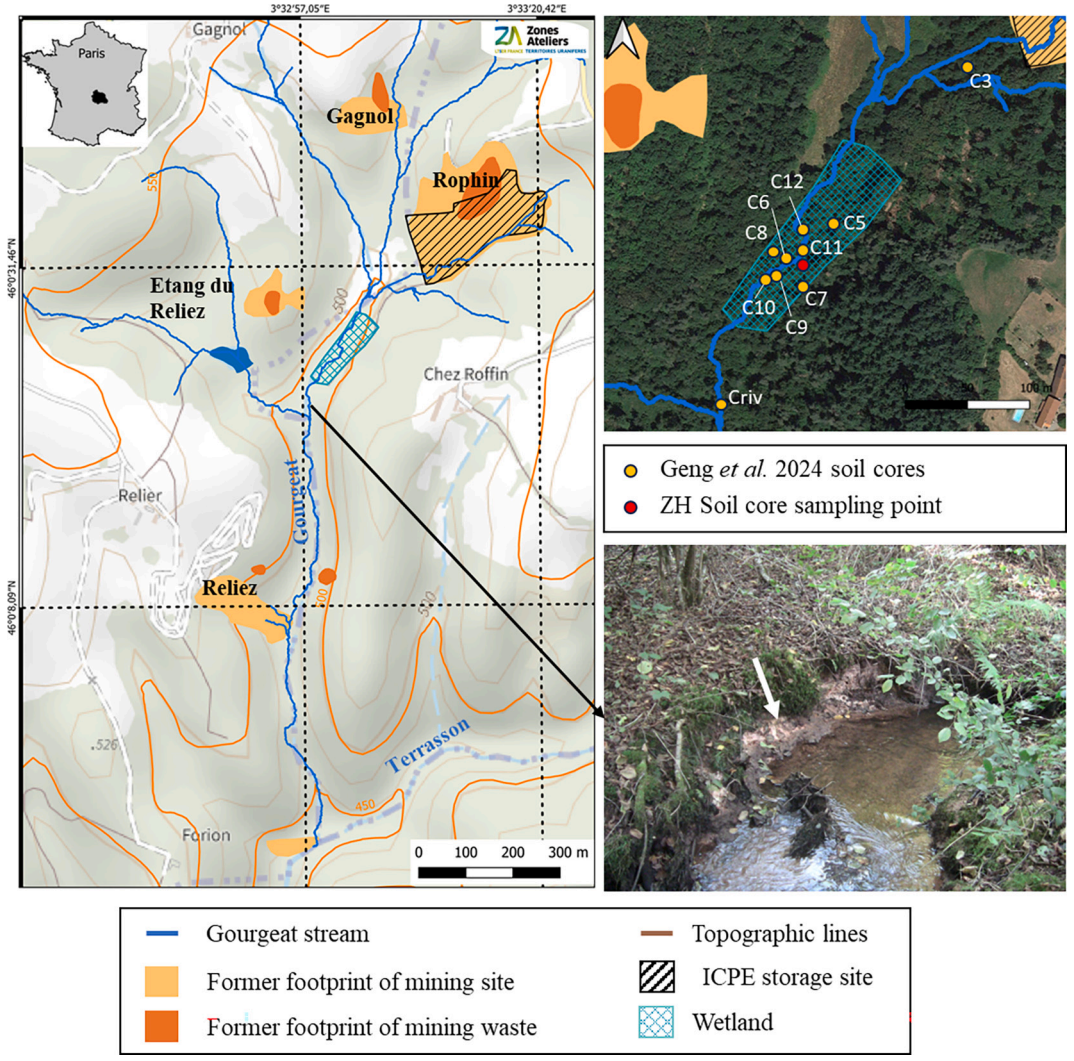

Fig. 1. Location of the ZH soil core relative to those studied by Geng et al. (2024). Photographs showed mining deposit (blank arrow) exposed along the bank of the Gourgeat stream.

above and below layers.

2.3. Reagents, materials, and solutions

Deionized water with a resistivity of 18.2 MΩ.cm was used to prepare aqueous solutions obtained from a Milli-Q system (Millipore). High purity acids obtained by distillation (Savillex® DST-1000 system) of HCl (Merck, EMSURE 37%) and HNO_3 (VWR Chemicals, NORMAPUR 68%) were also used.

The following chemical products were used in this study: hydrofluoric acid (VWR, Suprapur 40%) and perchloric acid (VWR Chemicals, NORMAPUR 70%), hydrogen peroxide solution (VWR Chemicals, NORMAPUR), glycerol (VWR Chemicals, NORMAPUR), glacial acid (VWR Chemicals, NORMAPUR), sodium citrate monohydrate salt (PROLABO, NORMAPUR), sodium bicarbonate salt (MERCK, Pro Analysis), acid ascorbic salt (PROLABO, NORMAPUR), sodium hydroxide salt (PROLABO, NORMAPUR), hydroxylamine hydrochloride (VWR Chemicals, NORMAPUR), ammonium acetate salt (Merck, EMSURE). For elemental analyses, a series of mono-standard solutions (VWR) were used for the preparation of home-made multi-standard solutions for elemental analysis: Fe, Mn, Mg, Si, Al, Ba, Ca, P, Cu, Zn, Pb, Th and As with an initial concentration of 1000 $mg.L^{-1}$ and U with an initial concentration of 10 $mg.L^{-1}$. Disposable polypropylene containers and/or conical tubes (VWR) were used in all experiments to ensure sample integrity and prevent contamination.

2.4. Elemental analysis of the samples

2.4.1. Soil treatment

After sampling, the water content (*W*) of the wetland soil was measured by gravimetry as the ratio of mass of water (M_{water}) to wet soil (M_{wet}). The soil samples were dried at 55 °C in a steam oven (VWR Venti-Line) until a constant mass was reached. The samples were stored in polypropylene containers at ambient temperature (20 ± 2 °C). All soil samples were finely ground in agate mortar prior to acid digestion, alkaline fusion, one-step and sequential extractions.

2.4.2. Loss on ignition, carbon, nitrogen and sulfur analyses

LOI was measured by heating pre-weighted dried samples in a muffle furnace at 550 °C for at least 5 h. The *LOI* percentage was calculated from mass loss, primarily attributed to the volatilization of organic matter. Total carbon (*TC*), total nitrogen (*TN*), and total sulfur (*TS*) contents of wetland soil samples were determined by CHNS analyses (FlashSmart, Thermo Scientific). Particulate inorganic carbon (*PIC*) and nitrogen (*PIN*) values, determined from calcinated samples (obtained during *LOI* measurement), were below the detection limits for all soil core samples indicating negligible inorganic contributions. Thus, *TC* and *TN* were considered to represent Particulate Organic Carbon (*POC*) and Nitrogen (*PON*) respectively, in this study.

2.4.3. Total acid digestion and fusion procedure

Total acid digestions of solid samples were performed to quantify their elemental composition. Briefly, 50 mg of finely ground samples (< 100 μm) were placed in a 20 mL PFA reactor (SAVILLEX) and successively attacked with concentrated HNO_3-HF-$HClO_4$ acids according to the method C described in the study of Yokoyama et al. (1999). The dry residues were finally treated with 5 mL of 3 $mol.L^{-1}$ HNO_3 solution.

Si contents were determined after alkaline fusion on soil samples according to the same procedure described previously (Darricau et al., 2024). Briefly, 150 mg of finely ground sample were placed on a 900 mg powder mixture of $LiBO_2$/LiBr (98.2 and 1.5% *w/w*, respectively; SPEX Fusion Flux, Pure) in a platinum crucible (5AUPTKAX, KITCO). The platinum crucible was heated in a Katanax K1 Prime furnace at 600 °C to oxidize the reduced elements and POM for 5 min, then at 985 °C during 10 min to fuse the sample. After cooling, the fusion melt was dissolved in 200 mL of 1.0 M HNO_3, 1.4 M H_2O_2 and 0.5 M glycerol solution, with dissolution aided by 2–5 min of ultrasonic treatment.

2.4.4. Chemical extractions for Cu, Fe, Pb and U

Three single-step extractions and a BCR-type sequential chemical extraction method were used on selected wetland soils according to geochemical index values (I_{geo}) (see Section 2.5 for more details) choose as an indicator of the various levels of metal enrichment. These complementary extraction methods were used to assess the partitioning of metals among different solid-phase fractions and to evaluate their potential mobility and environmental availability under changing geochemical conditions. The combination of these extractions and leaching allows to capture complementary aspects of U and metal reactivity. While sequential extraction provides information on operationally defined fraction, single-step and leaching tests offer estimation on the mobilizable pools under specific geochemical conditions. The combined application of multiple extraction strategies therefore enables a more comprehensive and chemically meaningful characterization by exploring complementary compartments rather than redundantly targeting the same fraction. It is acknowledged that sequential extraction schemes are subject to partial overlap between targeted phases (Cappuyns et al., 2007; Bacon and Davidson, 2008). During the different extraction steps, several processes can lead to redistribution of metals, including incomplete selectivity of reagents (depending on the metals), readsorption onto residual solid phases (*e.g.*, clays minerals, OM), or secondary precipitation (*e.g.*, Pb- or U-phosphates under acidic conditions). Consequently, redistribution of U and associated metals during extraction cannot be fully excluded and constitutes an inherent limitation of such approaches. Interpretations are thus based on comparative trends rather than absolute phase quantification, and are supported by complementary spectroscopic and microscopic analyses.

The two first single-step extraction procedures used were: (1) a Citrate Bicarbonate Ascorbate (CBA) solution for 24 h (pH = 7.5; $[NaHCO_3] = 0.6$ $mol.L^{-1}$; $[Na_3C_6H_5O_7] = 0.2$ $mol.L^{-1}$; $[C_6H_8O_6] = 0.1$ $mol.L^{-1}$; liquid/solid ratio of 25: 1, 24 h) to extract metals associated with easily reducible amorphous Fe(III) and Mn(III/IV) oxyhydroxides (Haese et al., 2000; Hyacinthe et al., 2006; Hyacinthe and Van Cappellen, 2004); and (2) 1 $mol.L^{-1}$ HCl (liquid/solid ratio of 20: 1, 24 h) to extract exchangeable species and those bound to POM, amorphous and poorly crystalline Fe(III) and Mn(III/IV) oxyhydroxides, carbonates, phosphates and reactive sulfides (Cooper and Morse, 1998; Larner et al., 2006; Leleyter et al., 2012; Ruban et al., 2001; Yu et al., 2021). A third single-step extraction was performed using the NF EN 12457-2 leaching test to quantify the easily extractable metal fraction and assess environmental compliance with European waste criteria (Foucault et al., 2012). Samples (500 mg) were incubated for 24 h with deionized water (pH = 5–7.5; conductivity < 0.5 $\mu S.cm^{-1}$; liquid/solid ratio of 10:1). Mixtures were vigorously shaken on an orbital shaker (200 rpm; BIOBLOCK scientific) and filtered through 0.45 μm cellulose acetate membranes. Residual solids were collected and dried for mineralogical analyses of the residual metal-bearing phases.

In addition to single-step extraction experiments, a modified BCR sequential extraction procedure (Mossop and Davidson, 2003; Pérez-Moreno et al., 2018; Ruban et al., 2001) was used on 250 mg samples to evaluate metal partitioning. The four steps targeted were: F1 the exchangeable/acid-soluble metals with 0.11 $mol.L^{-1}$ acetic acid (16 h); F2 the reducible fraction with 0.5 $mol.L^{-1}$ hydroxylamine chlorohydrate (16 h); F3 the oxidizable fraction with 8.8 $mol.L^{-1}$ H_2O_2 (1 h at room temperature, then 1 h at 85 °C, to reduce at 1 mL), followed by 1 $mol.L^{-1}$ ammonium acetate at (16 h); and F4 the residual fraction after total acid digestion. Recoveries for Cu, Pb, and U were acceptable (Table S1). The percentages represented the proportion of each extracted element content ($\{X\}_{extracted}$, $mg.kg^{-1}$) compared to the bulk element value ($\{X\}_{bulk}$) $mg.kg^{-1}$ using $\%_{extracted} = \{X\}_{extracted}/\{X\}_{bulk} \times 100$, where *X* corresponded to the targeted metal. It provides a quantitative estimate of the mobility or association of the metals with specific geochemical fractions

under different pH and redox conditions.

All extraction and leaching experiments were conducted in duplicates except for the BCR extraction, which were performed in triplicate. Reported values represent mean concentrations, with standard deviations shown in figures and tables.

2.4.5. Elemental analysis

Depending on the concentration level, the total element concentrations in diluted extracts (at least 100- and 1000-fold dilution made for alkaline fusion and single-step extraction with 0.3 mol.L^{-1} HNO_3 solution to avoid matrix effects) were analyzed by ICP-OES (Thermo Fisher ICAP™ 7600 Duo) or ICP-MS/MS (Agilent 8800, Agilent Technologies). Calibrations were performed with multi-standard solutions in matrices similar to the diluted extracts, with $R^2 > 0.995$. Blank correction was applied when necessary, and quality control solutions were regularly analyzed. Reference materials (SARM Granites GA (Govinoaraju and De La Roche, 1977) and Tibet Sediment NCS DC 70317 (Ferrari et al., 2021)) were used as total digestion controls. Acceptable recovery (80–120%) was obtained using both acid digestion and alkaline fusion (Chang et al., 2009). Instrumental detection and quantification limits for each element are provided in Table S2 and S3. Stable Pb isotope ratios were calculated directly from the ICP-MS/MS measurements, without preliminary chemical separation of Pb from the matrix and without applying instrumental mass fractionation correction. Although this approach is less rigorous than standard protocols it was sufficient to identify isotope trends and distinguish potential Pb sources in the context of this study. SIMS analyses will be used to further refine the origin of U-bearing minerals (Section 2.7).

2.5. Geochemical index methods

Geoaccumulation index (I_{geo}) was used previously to estimate metal enrichment compared to a natural geochemical background (*i.e.*, not contaminated or polluted) and identify anthropogenic-impacted zones (Rubio et al., 2000; Sakan et al., 2015). Calculations and data analyses are described in the Supplementary Material. Background levels were calculated from metal contents in the ZH3 paleosoil layer, which was previously dated using ^{14}C by Martin et al. (2020), formed before the beginning of U mining activities and thus considered not impacted by U mining activities.

2.6. Mineralogical analyses

Major mineral phases were characterized by bulk powder XRD (0–80°X 2θ, $CuK_\alpha = 1.5418$ Å, step size 0.017°, scan step time 775.335 s) on a Panalytical diffractometer at GEOPS facility (Orsay, France). Clay minerals were analyzed by the Stoke's law fractionation method. For SEM and EPMA, soil and sediment samples were embedded in an Epoxy resin (EpoFix, Struers) prior analysis. Secondary electron images were obtained with SEM Phenom™ Pro X at GEOPS facility (Orsay, France) equipped with an EDX probe (15 keV). EPMA analyses were performed on SEM-selected particles (15 kV, 4-nA beam current) on a CAMECA SX Five (Camparis, UMPMC, France) calibrated with certified standards (Ecce Terra, 2018). Two to three analyses were carried out on each particle to improve counting statistics. The XRD patterns were used to broadly identify the main mineral groups present and to contextualize the geochemical environment, rather than to achieve full crystallographic resolution of clays. SEM-EDS was then employed to locate and observe U-bearing and accessory phases, while EPMA provided quantitative confirmation of their composition.

2.7. Radiogenic Pb detection and location by SIMS

SIMS analyses of Pb-rich phases were conducted using a CAMECA IMS7 F-E7 (PATERSON Platform, ASNR, Fontenay-aux-Roses). "Radiogenic" refers to Pb produced by the U-decay (uranogenic). Imaging aimed to identify the radiogenic Pb-bearing phases (*i.e.*, ^{206}Pb-rich and ^{208}Pb-poor) at the grain scale. Samples were introduced into the analysis chamber (pressure of 5×10^{-9} mbar) using a 5 nA, 12 kV O_2^- primary beam projected on a ~ 1 µm area which scanned the area of interest (a raster of 250 µm × 250 µm for the mining deposit sampled at 16–18 cm depth). The positively charged secondary ions or molecules were accelerated at 10 kV into the mass spectrometer, measured with a mass resolution of 400 by ion counting in monocollection mode and sequentially converted into an image with a lateral resolution of around 1 µm. Prior to each analysis, a 5-min pre-sputtering procedure was conducted using a primary beam of approximately 100 nA. The analysis includes 500 integration cycles, each lasting 10 s for $^{206}Pb^+$, $^{207}Pb^+$, $^{208}Pb^+$, and $^{238}U^{16}O^+$, and 1 s for $^{28}Si^+$. Mass calibration used a Pb-rich metal (common Pb isotopic signature) and a Si plate.

2.8. Micro X-ray fluorescence and X-ray absorption near-edge structure

2.8.1. µ-XRF and Cu K-edge µ-XANES analysis on PUMA

µ-XRF mapping and Cu K-edge µ-XANES analyses were conducted on the 16–18 cm depth sample from the ZH2 layer at the SOLEIL PUMA beamline (Saint-Aubin, France). The standards/samples preparation, the acquisitions, and the results were consistent with those acquired in the study of Darricau et al. (2024). The reference samples included Cu oxide, Cu-foil, CuS, Cu_2S, $CuSO_4$, shattuckite ($Cu_5(SiO_3)_5(OH)_2$), kobyashevite ($Cu_5(SO_4)_2(OH)_6 \bullet 4H_2O$), chalcanthite ($CuSO_4 \bullet 5H_2O$), yvonite ($Cu(AsO_3OH)$), pushcharovskite ($Cu(AsO_3OH) \bullet 1.5(H_2O)$), azurite ($Cu_3(CO_3)_2(OH)_2$), malachite ($Cu_2CO_3(OH)_2$), $CuCO_3$, Cu diacetate, CuF_2, $CuCl_2$. In addition, the following synthesized materials were also measured: doped goethite with 0.7 wt% Cu and 0.5 wt% Cu and doped ferrihydrite with 0.3 wt% Cu and 0.5 wt% Cu.

2.8.2. µ-XRF and Pb L_{III}-edge µ-XANES analysis on Diffabs

µ-XRF mapping and Pb L_{III}-edge µ-XANES analyses of samples from the horizon "1" and "2" from the soil core ZH were conducted at the SOLEIL beamline DiffAbs (Saint-Aubin, France). The X-ray incident beam was monochromatized using a Si(111) double crystal. Kirkpatrick-Baez focused the beam down to 11.1H * 5.67 V µm. The XANES spectra were calibrated thanks to a pure metallic Pb foil. Various sizes of µ-XRF maps were acquired with a counting time of 0.1 s per point and a step size between 50 and 12 µm in continuous scanning mode (flyscan; Leclercq et al., 2015). Finally, Pb-rich areas of interest were analyzed by µ-XANES at the Pb L_{III}-edge. The µ-XANES spectra were then analyzed using the ATHENA software analysis (Ravel and Newville, 2005). Linear Combination Fitting (LCF) was performed to estimate the content of each component. References spectra were acquired for sample Pb-speciation identification and LCF calculations: Pb_3O_4, PbO, $Pb_3O_2P_4$, $PbHPO_4$, $PbCO_3$, $PbSO_4$, and Pb Azelate (PbAz). Fig. S7 displays the reference spectra acquired. The µ-XANES spectra were also compared with previously published reference compound spectra (Cervi et al., 2021; England et al., 1999; Feng et al., 2022; Mikhlin et al., 2021; Ohta and Kubota, 2016; Sekine et al., 2017).

All µ-XANES spectra were fitted over the energy range chosen for Cu K-edge (8960–9100 eV) and Pb L_{III}-edge (13,070–13,210 eV) using linear combination fitting (LCF). Energy calibration was performed using reference standards. The quality of the linear combination fitting (LCF) was evaluated using the reduced chi-square ($\chi^2 R$) and the R-factor (Rf), which quantify the agreement between experimental and fitted spectra, with lower values indicating a better fit (good with Rf < 0.01–0.02; acceptable with Rf between 0.02 and 0.05).

3. Results and discussion

3.1. Wetland soil characteristics

The depth profiles for *LOI*, *TC*, *TN*, water content, and elemental composition enabled the distinction of three well-defined geochemical

layers within the "ZH" soil core. These stratigraphic divisions were clearly presented in Table 1 and thoroughly detailed in the supplementary data information (Table S4). They reflected variations in both organic matter content and mineralogical composition throughout the ZH soil core.

Layer ZH1 exhibited high TC contents with a terrigenous signature ($TC/TN > 10$). XRD analysis revealed a mineral composition of quartz, albite, microcline and muscovite (Fig. S1) – consistent with chemical data (Table 1) and the site's granitic geology. The organic-rich ZH1 horizon overlayed a mainly mineral silty-loamy layer ZH2.

Layer ZH2, identified as "mining deposits" (Martin et al., 2020; Geng et al., 2024), was considered as the primary source of ^{238}U and ^{235}U decay-series nuclides and co-occurring metals in the wetland. These materials originated from the discharges of U mining water discharge and/or runoff nearby settling ponds. The isotopic ratios of $^{206}Pb/^{208}Pb$ confirmed that the mining deposits originated from the two types of U ores treated in the Rophin washing plant: Rophin and BNL. ZH2 was *POC*-depleted and composed of minerals, containing clay minerals (vermiculite, muscovite and kaolinite), quartz, and K-feldspar (Table 1, Fig. S1).

Finally, layer ZH3 corresponded to the original soil predating U mining (Table 1). It showed higher *TC*, *LOI*, and water content than ZH1, consistent with its lower mineral fraction (Table 1, Fig. S1). The main features of the studied core aligned with those previously sampled in the Rophin wetland (Martin et al., 2020; Geng et al., 2024; Montavon et al., 2025). To better understand the origin of co-occurring metals, the source of U was further examined in the next section.

3.2. Origin of U in mining deposits

3.2.1. Detection of radiogenic Pb

To determine the origin of U in mining deposits, U-bearing phases were identified by SEM, combined with $^{206}Pb/^{208}Pb$ ratios and chemical analyses. Geng et al. (2024) reported two different Pb sources related to the core sampling location in the wetland soils (Fig. 1): a non-radiogenic ($^{206}Pb/^{208}Pb \approx 0.48$) linked to Rophin parsonsite ($Pb_2(UO_2)(PO_4)_3$) ores, and a radiogenic one from the chemical treatment of BNL pitchblende (UO_2) ores (Section 2.1). Due to the large isotopic contrast between the two endmembers, bulk analyses (*i.e.*, without chemical separation) allowed to distinguish the different U-mining inputs in wetland soil samples. $^{206}Pb/^{208}Pb$ ratios in sample from 8 to 11 and 11–14 cm depth exceeded the Present-Day Average Crustal (PDAC) value of 0.48 (Cumming and Richards, 1975), indicating a radiogenic Pb signature (Fig. 2, Table S4).

3.2.2. BNL origin

SEM observations revealed lumpy and fine-grained U oxides, with Pb contents up to 4.6 wt%, suggesting an authigenic origin in mining deposits sampled at 11–14 and 16–18 cm depth (Fig. S2). These deposits exhibited high U contents (1077 and 1106 $mg.kg^{-1}$) (Table S5). SIMS imaging of U rich hot spots revealed $^{206}Pb/^{208}Pb$ ratios of 0.9–1.0 – higher than the PDAC value (0.48) and lower than the radiogenic Pb signature of the pitchblende ore ratio of 7.7 (Geng et al., 2024) (Fig. 3). The intermediate values could support the hypotheses of the formation of authigenic U oxides through oxidation-driven redistribution from the BNL pitchblende source, likely triggered by water table fluctuations. A BNL ore-treatment origin from the mining deposits recorded from 11 to 18 cm depth is the most possible. This was supported by Geng et al. (2024), who identified a radiogenic Pb signature in U oxides from the BNL pitchblende ore.

3.2.3. Rophin origin

In contrast, SEM observations of the soil core sample at 18–20 cm showed very sparse U-oxides, and no U-bearing crystalline minerals at 20–22 cm depth (Fig. S2). Moreover, these two layers revealed higher U contents (1321–1616 $mg.kg^{-1}$) compared to the BNL-related layer (810–1076 $mg.kg^{-1}$). The common Pb signature ($^{206}Pb/^{208}Pb \approx 0.5$) for these two samples and the U/Pb mass ratio of 0.5 in agreement with the parsonsite stoichiometry, indicated that this layer could be derived from the physical processing of parsonsite ores. Finally, parsonsite crystals were barely observed by SEM (only two crystals) in the 16–18 cm layer (Fig. S2-b). The coexistence of two different U-rich minerals indicated that this layer could be considered as a mixture of the two above-mentioned U sources.

3.2.4. Vertical partitioning of mining deposits

The results enabled the identification of three sublayers within mining deposits (ZH2): i) 10–14 cm depth, U primarily derived from the processing of BNL ores; ii) 14–18 cm depth, a mixture of both U sources; and iii) 18–22 cm depth, U predominantly from the parsonsite ore treatments.

3.3. Metal enrichment indexes

Metal enrichments in the ZH core were assessed using I_{geo} factor (Fig. 4). The top 30 cm showed enrichments for Zn, Cu, Pb, and U ($I_{geo} > 1$). The strongest U enrichment ($I_{geo} > 5$) occurred at 5–8 cm depth in the organic-rich ZH1 layer (13.7 wt%) and at 18–20 cm depth, reflecting the signature of Rophin U ore treatments.

Peaks of Cu and Pb enrichment ($I_{geo} > 4$) were observed at 11–14 and 18–20 cm depth, respectively (Fig. 4). SEM revealed chalcopyrite crystals only in the BNL-derived sublayer (ZH2) and in the mixing zone (14–18 cm), associated with U oxides (Fig. 5-d, Table S6). This aligns with historical studies identifying chalcopyrite as the main sulfide phase in the third mineralogical event for the BNL mineralization (Section 2.1; Cuney, 1978). For Pb, this enrichment could be attributed to the prevalence of plumbogummite $PbAl_3(PO_4)_2(OH)_5{\bullet}(H_2O)$ crystals in the Rophin-derived ZH2 sub-layer. I_{geo} values for Zn indicated moderate to high enrichment at 18–22 cm depth. SEM observations of the 18–20 cm layer revealed rare sphalerite (ZnS) crystals. The presence of Rophin-derived materials, along with the absence of a discernible Zn in BNL-derived materials, suggested that Zn could be a valuable proxy of

Table 1
: Main physicochemical and mineralogical characteristics of the three layers composing the ZH soil core. Total carbon (TC) and total nitrogen (TN) were used as proxies for particulate organic carbon (POC) and nitrogen (PON), respectively, due to negligible inorganic contributions. Further details are displayed in the Supplementary Material (Table S4). The classification of particulate organic matter (POM) follows the criteria established by Seeber and Seeber (2005).

Layer	Textural composition	Observations	Mean chemical content (wt%)								Classification of POM
			SiO_2	Al_2O_3	Fe_2O_3	MgO	*LOI*	Water	*TN*	*TC*	
ZH 1 (1.5–11 cm depth)	Organic layer	Black soil with fibrous organic material (such as roots and leaf)	59.7	12.26	1.75	0.34	33.5	65.4	1.11	13.7	$TC/TN > 10$ terrigenous
ZH 2 (11–20 cm depth)	Silt loam texture	Whitish color	85.4	13.58	1.07	0.37	6.4	36.4	0.12	1.9	$TC/TN > 10$ terrigenous
ZH 3 (20–50 cm depth)	Organic layer	Dark brown soil	37.4	8.96	1.25	0.19	58.1	73.3	1.75	28.7	$15 < TC/TN < 20$ soils of untended forests POM more heavily decomposed

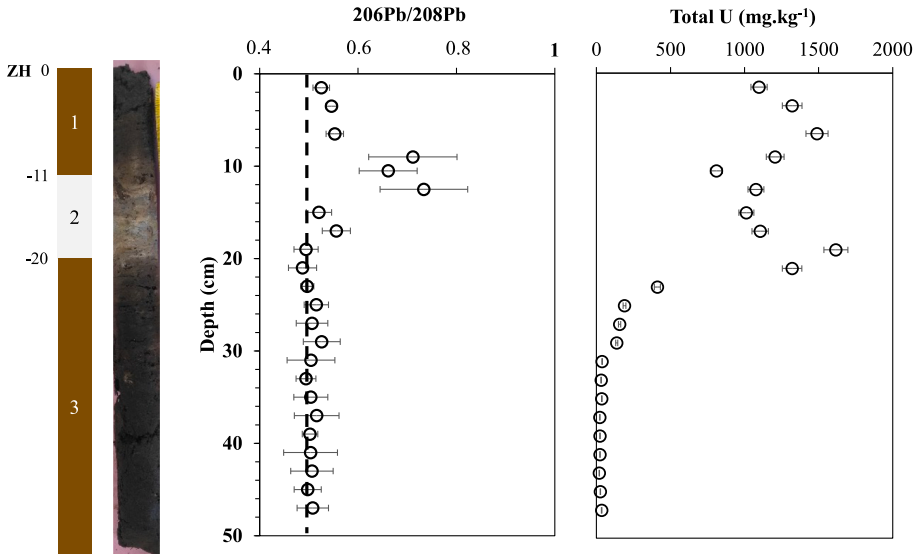

Fig. 2. $^{206}Pb/^{208}Pb$ ratios and total U contents plotted by depth in the ZH soil core. The dotted line represents the PDAC signature of 0.48 (Cumming and Richards, 1975). The distinction of three well-defined geochemical layers within the "ZH" soil core was explained in Section 3.1.

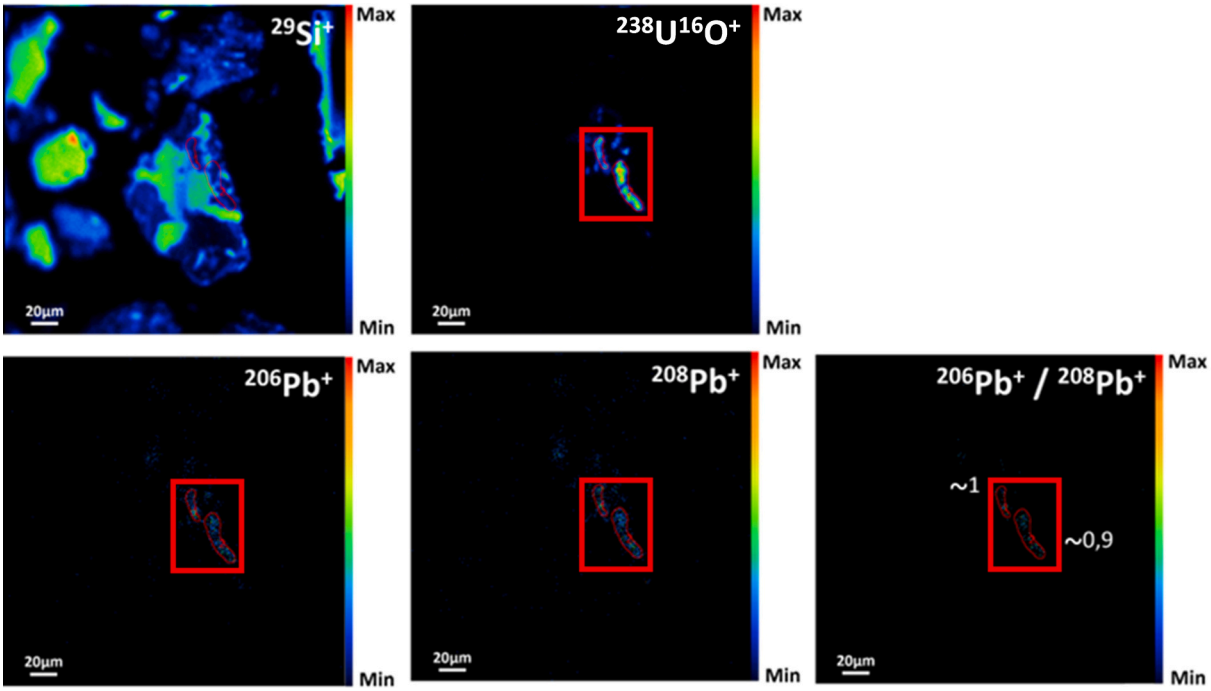

Fig. 3. SIMS images showing the spatial distribution of $^{29}Si^+$, $^{238}U^{16}O^+$, $^{206}Pb^+$ and $^{208}Pb^+$ in mining deposits sampled at 16–18 cm depth.

Rophin ore influence. As noted, two sub-layers contained mining materials from distinct types of U ore treatments. The next section focused on the solid speciation of U, Cu and Pb in mining materials, the surface layer (ZH1) and original soil (ZH3), to understand their behavior and mobility under oxidizing conditions.

3.4. Metal speciation in the various soil layers

3.4.1. Uranium speciation in soil layers

A significant U fraction (74–89% of total U content) was extracted with 1 $mol.L^{-1}$ HCl from the different soil layers (ZH1, ZH2 and ZH3), while the CBA agent extracted 51–89% of total U (Fig. 6). Bicarbonate ligands were known to effectively mobilize sorbed U(VI) and U(IV) in soils and sediments, under both anoxic and oxic conditions due to their strong affinity for U (Langmuir, 1978; Alessi et al., 2012; Zhou and Gu, 2005). Furthermore, the BCR F3 step, targeting the oxidizable fraction bound to POM, extracted 70–88% of the total U content in the *TC*-rich layers (ZH1 and ZH3; Fig. 6). This strong U-POM association had been reported in both impacted and natural wetland (Martin et al., 2020, 2021; Grangeon et al., 2023; Stetten et al., 2018b; Lefebvre et al., 2022; Regenspurg et al., 2010).

About 59% of total U was extracted by the BCR F1 step in the BNL-derived ZH2 sub-layer, indicating that a large pool of easily extractable species (Fig. 6) is likely adsorbed onto clay minerals (Bartl and Czurda, 1991; Davey and Scott, 1956; Syed, 2006). In contrast, for the same fraction, only 18% of total U were found from the Rophin-derived sub-layer (18–20 cm depth), which contained significantly more *POC* (20 wt% *vs* 2 wt%), suggesting stronger U-POC binding and greater

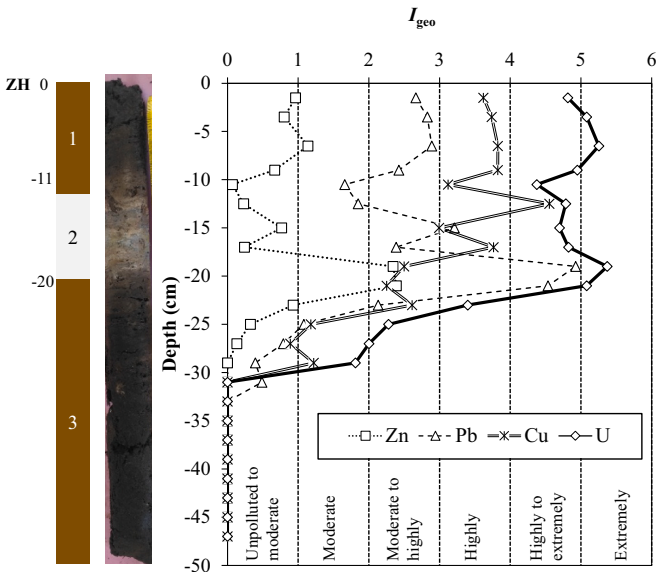

Fig. 4. Geoaccumulation index (I_{geo}) values for Zn, Pb, Cu, and U measured along the ZH soil core depth profile. The distinction of three well-defined geochemical layers within the "ZH" soil core was explained in Section 3.1.

retention. SEM observations after BCR F1 and F2 steps confirmed that U oxide crystals in the BNL-derived sub-layer, though abundant, accounted for only ≈ 10% of total U (Fig. S5 and S6).

In summary, U speciation in ZH1 and ZH3 layers was mainly dominated by sorbed forms, linked to POM. In ZH2 layer, higher U extraction in BCR F1 and F2 step indicated more easily extractable U species. To a lesser extent, authigenic and/or originated U oxides from treated BNL ores were observed in the BNL-derived ZH2 sublayer, along with rare U (VI)-phosphate phases like parsonsite (SEM-EDS analyses). Finally, minor amounts of refractory U-rich minerals, including zircon and REE-phosphate species, were detected throughout the soil core.

3.4.2. Lead speciation in soil layers

Numerous small-sized plumbogummite crystals (2 to 5 μm), containing traces of Fe (Fig. 5a) were especially observed in the Rophin-derived sublayer. XANES analyses of Pb-rich particles in ZH1 and ZH2 layers (Fig. 8, Table S9), localized *via* μ-XRF maps (Fig. 7a and S8), closely matched with the reference Pb phosphates *i.e*, compound $Pb_3O_2P_4$ (Chi^2_R = 0.025; Fig. S7). Other Pb-bearing phases were less identified, including galena, pyrite and Ti oxides with U and Pb contents of 1–30 wt% and 1.6–13.5 wt%, respectively (Fig. 5 and Table S5). The presence of Pb-rich sulfate minerals such as anglesite (sometimes Cu- and As-enriched) and Pb-rich barite were also confirmed by LCF fits (Fig. 8a and b, Table S7, S8) and SEM (Fig. 5-c, Table S5). These results aligned with previous reports of anglesite in Zn-ore process waste or in Ag—Pb mine tailings as a stable secondary phase (Audry et al., 2010; Courtin-Nomade et al., 2016; Gieré et al., 2003). Finally, μ-XANES spectra from mining deposit layer at 16–18 cm depth resembled Pb Azelate ($C_9H_{14}O_4Pb$), used as organic Pb complexes (Fig. 8c, Table S9) (Morin et al., 1999).

A significant Pb fraction (58–75% of the total Pb content) was extracted with 1 mol.L^{-1} HCl from the various soil layers (ZH1, ZH2 and ZH3; Fig. 6). After the extraction, SEM observations revealed the absence of Pb-rich phosphate and sulfate minerals, suggesting that these phases are potentially soluble in 1 mol.L^{-1} HCl. However, these results should be interpreted with caution. Wei et al. (2005) suggested that using 0.1 mol.L^{-1} HCl could underestimate Pb availability due to its precipitation as cotunnite ($PbCl_2$) (Wei et al., 2005). However, no evidence of this compound was observed by SEM in the post-extraction samples.

The CBA agent extracted 8–21% of total Pb, mainly from the Rophin sub-layer and ZH1 layer (Fig. 6). In ZH2 layer, Pb extraction was 4% for the BNL-derived sublayer *versus* 28% for the Rophin-derived sublayer, which also shows higher Pb (> 3200 mg.kg^{-1}) and POC (20 wt%) contents. This could explain the Pb accumulation in the Rophin-derived sub-layer through adsorption onto organic surfaces or the formation of organo-metallic complexes.

The BCR F2 step, targeting metals associated with amorphous and

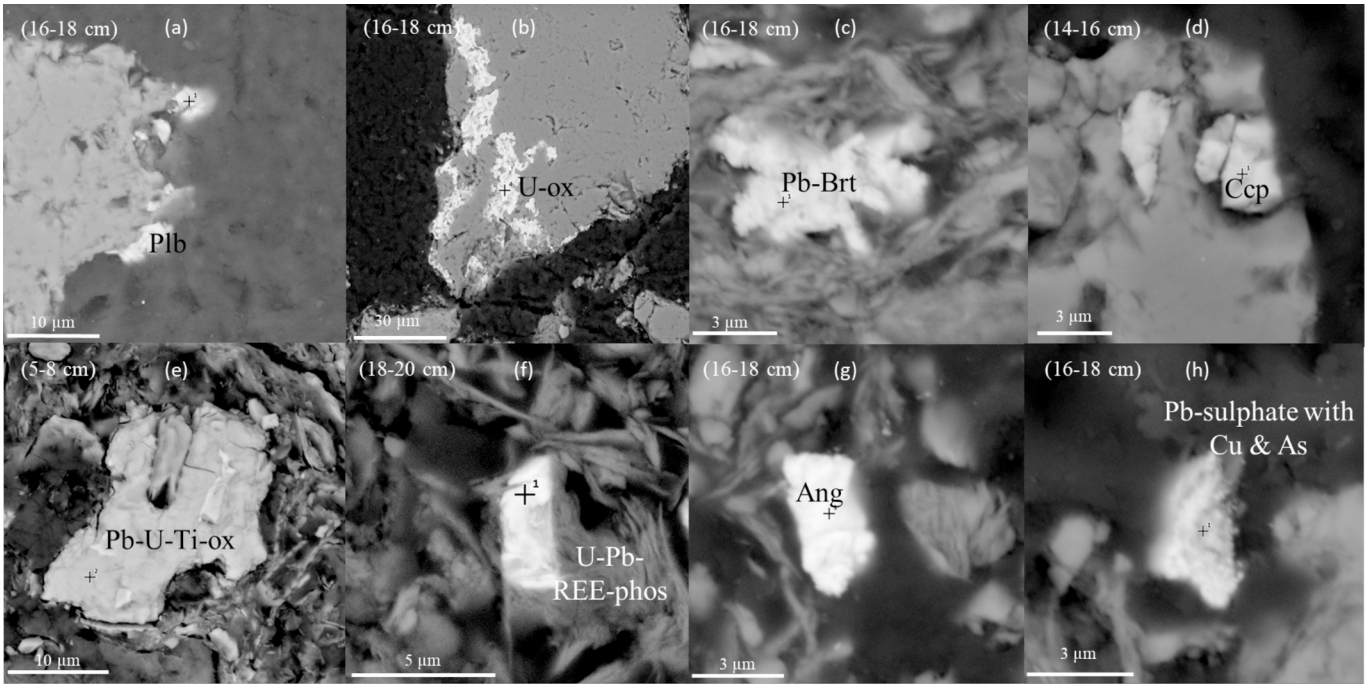

Fig. 5. SEM images of minerals identified in ZH soil samples at various depth (depths indicated for each images): (a) plumbogummite (Plb), (b) U-oxide (U-ox), (c) Pb-barite (Pb-Brt), (d) Chalcopyrite (Ccp), (e) Ti-oxide with U and Pb (Pb-U-Ti-ox), (f) REE phosphate with U and Pb (U-Pb-REE-phos), (g) anglesite (Ang) and (h) other Pb-sulfate enrich in Cu and As. EDX spectra associated to SEM image (b), (e), (f) and (h) are displayed in Fig. S3.

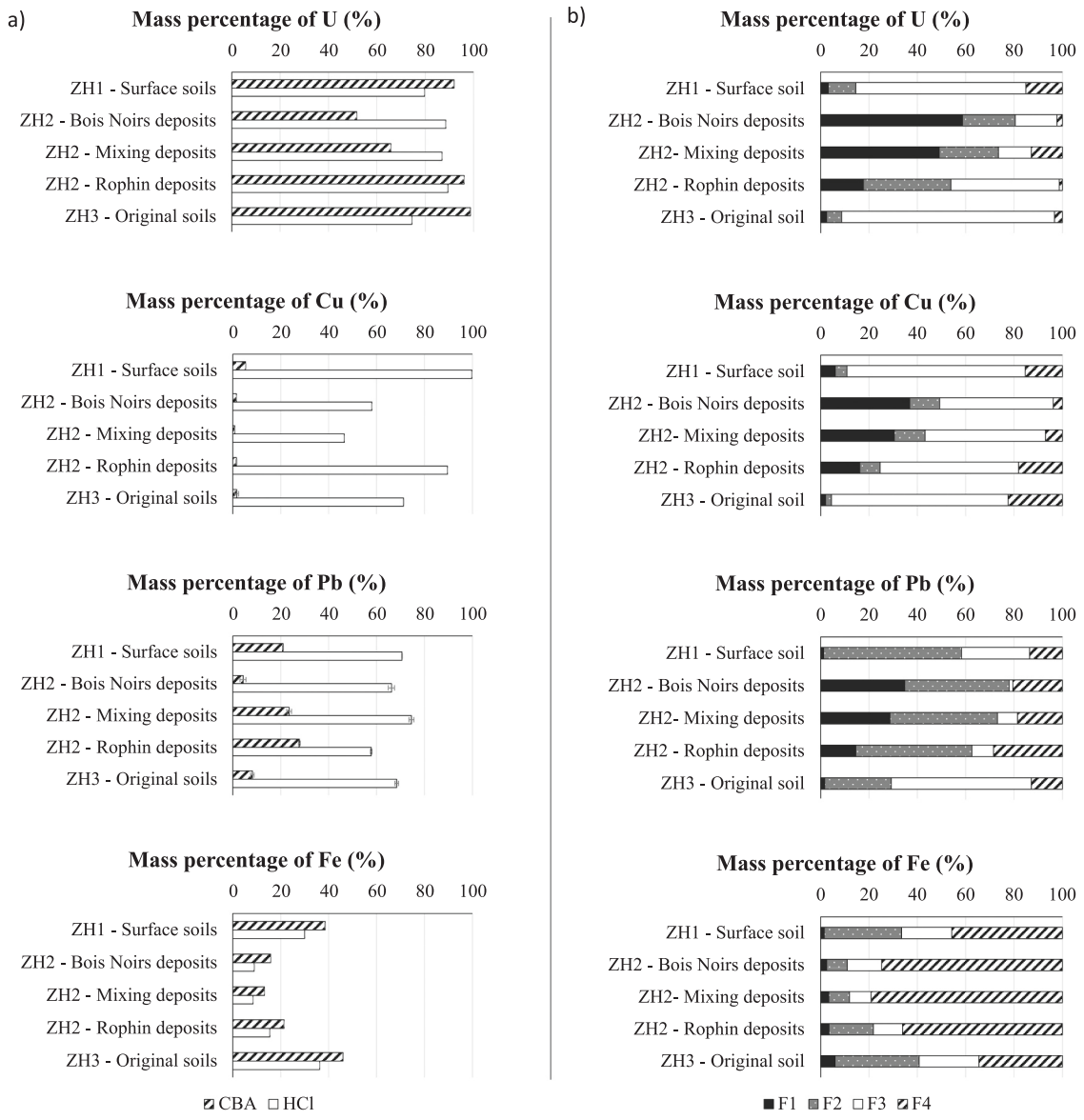

Fig. 6. Mass percentages of U, Cu, Pb, and Fe relative to their initial total content in the selected ZH core bulk samples at various depths, determined by a) CBA and 1 mol.L^{-1} HCl single-step extraction and b) the BCR sequential extraction. These values represent the proportion of each metal associated with operationally defined geochemical fractions, reflecting their potential mobility and environmental availability.

poorly crystalline Fe(III) and Mn(III/IV) oxyhydroxides, extracted 30–60% of total Pb (Fig. 6), indicating these phases act as Pb sinks. However, previous studies showed that the BCR F1 and F2 step can lead to the dissolution of other Pb species, including anglesite ($PbSO_4$) or even Pb associated with POM (Cappuyns et al., 2007; Courtin-Nomade et al., 2016; Fanfani et al., 1997; Mossop and Davidson, 2003; Raksasataya et al., 1996; Tessier et al., 1979), due to hydroxylamine hydrochloride at pH 2 promoting Pb desorption with chloride ions. This could result in an overestimation of Pb associated with the exchangeable phase and oxyhydroxides.

The BCR F3 step yielded only minimal Pb extraction from the BNL-derived sublayer (Fig. 6), likely due to low POC, the presence of poorly soluble Pb minerals (Ti oxides, REE phosphates) and few sulfide phases (Fig. 8b - spectra I). In contrast, 28–58% of total Pb were extracted by the BCR F3-step in POC-rich layer (ZH1 and ZH3; Table 1 and Fig. 6). In addition, the μ-XANES spectrum of the bulk ZH1 layer at 6.5 cm depth matched the reference compound PbAz ($Chi^2_R = 0.018$) (Fig. 8d R) indicating significant Pb association with POM as observed in contaminated floodplain soils with low Pb partitioning in the aqueous phase (de Matos et al., 2001; Dewey et al., 2021).

In summary, Pb species were mainly easily extractable forms linked to POM in ZH1 and ZH3 layers, and possibly to mineral fractions (reducible Fe/Mn oxyhydroxide phases and clay) in ZH2 layer (mining deposits). Additionally, refractory crystalline minerals, including plumbogummite, Pb-rich barite and sulfide minerals were identified, along with inherited minerals from granite weathering and former U mining activities.

3.4.3. *Copper speciation in soil layers*

The μ-XRF Cu maps of the ZH2 layer revealed high-grade Cu particles measuring 8–250 μm (Fig. 7b). Although standard Cu μ-XANES spectra for chalcopyrite were not recorded, the Cu μ-XANES spectra 3, 4 and 5 in Fig. 9 were attributed to these species based on SEM observations and the typical Cu pre K-edge and K-edge for standard spectra (8979 and 8986 eV) from previous studies (England et al., 1999; Nevidomskaya et al., 2021; Ohta and Kubota, 2016). Small-size (3–5 μm) chalcopyrite ($CuFeS_2$) crystals were observed at 11–14 cm depth in the ZH2 layer (Fig. 5), where Cu enrichment was particularly significant ($I_{geo} > 2$;

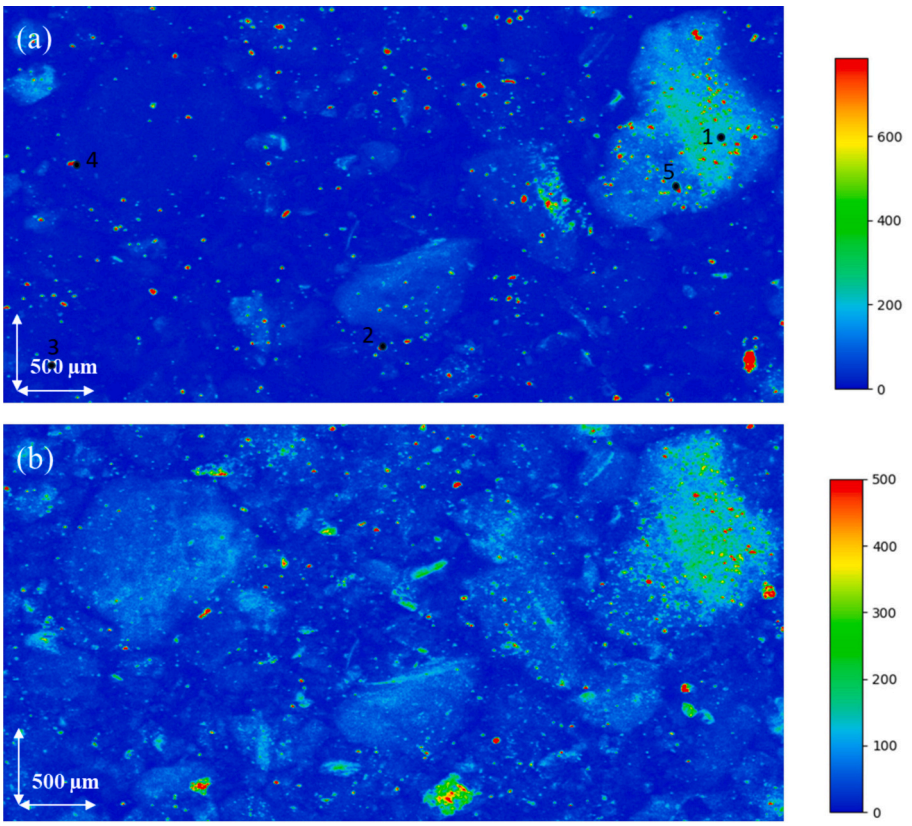

Fig. 7. Pb (a) and Cu (b) µ-XRF maps of the mining deposit sample at 16–18 cm depth. Areas with the highest concentrations appeared are shown in red, and the lowest in blue. (For interpretation of the references to color in this figure legend, the reader is referred to the web version of this article.)

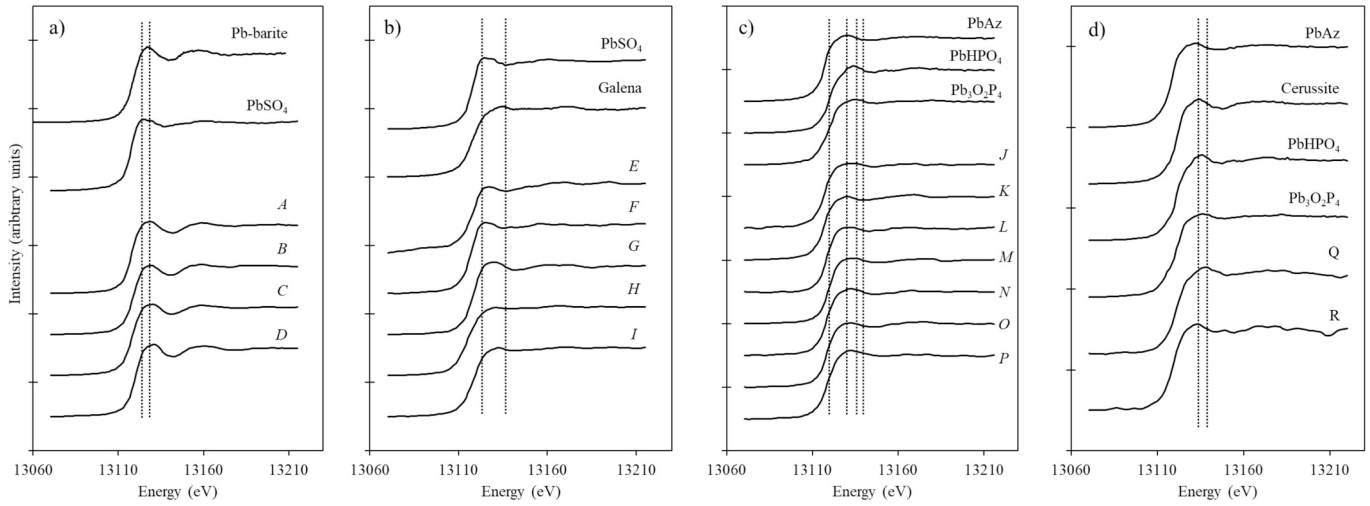

Fig. 8. Pb L^{III}-edge µ-XANES spectra A to P obtained for particles in the layer ZH2 at 16–18 cm depth, and Pb-LIII-edge µ-XANES spectra Q to R for particles in the layer ZH1 at 5–8 cm depth. The dotted lines highlight the differences in characteristics between the reference spectra.

Fig. 4). The Cu µ-XANES spectra 1 and 2 (Fig. 9a and b), the pre-edge at 8979 eV disappeared, suggesting chalcopyrite oxidation (England et al., 1999; Liu et al., 2015). Furthermore, the BCR F3 step extracted 47–57% of total Cu from ZH2 layer (mining deposits). Post-extraction SEM analyses of solid residues confirmed extraction of copper sulfide minerals consistent with its known ability to oxidize refractory sulfide species, such as chalcopyrite (Cardoso Fonseca and Martin, 1986). The 1 $mol.L^{-1}$ HCl extraction from the ZH2 layer (mining deposits) mobilized 46–89% of total Cu (Fig. 6). Post-extraction SEM analyses revealed partial dissolution of chalcopyrite crystals, as evidenced by etching and surface alteration features (Fig. S4). Although copper sulfide compounds, such as covellite (CuS), chalcocite (CuS_2), chalcopyrite ($CuFeS_2$) and pyrite (FeS_2) are generally poorly soluble in HCl solution at various concentrations (0.5–6 $mol.L^{-1}$) (Cooper and Morse, 1998; Heron et al., 1994; Praharaj and Fortin, 2004; Ueshima et al., 2019).

Chemical extraction experiments targeting Cu associated to reducible Fe/Mn oxyhydroxides showed very low contents: 0.8–5.4% and 8–13% for the CBA and BCR F2 step, respectively. However, Cu in sulfate minerals could have also been dissolved during these extractions (Macías et al., 2017). The BCR F1 step yielded more Cu from the BNL-

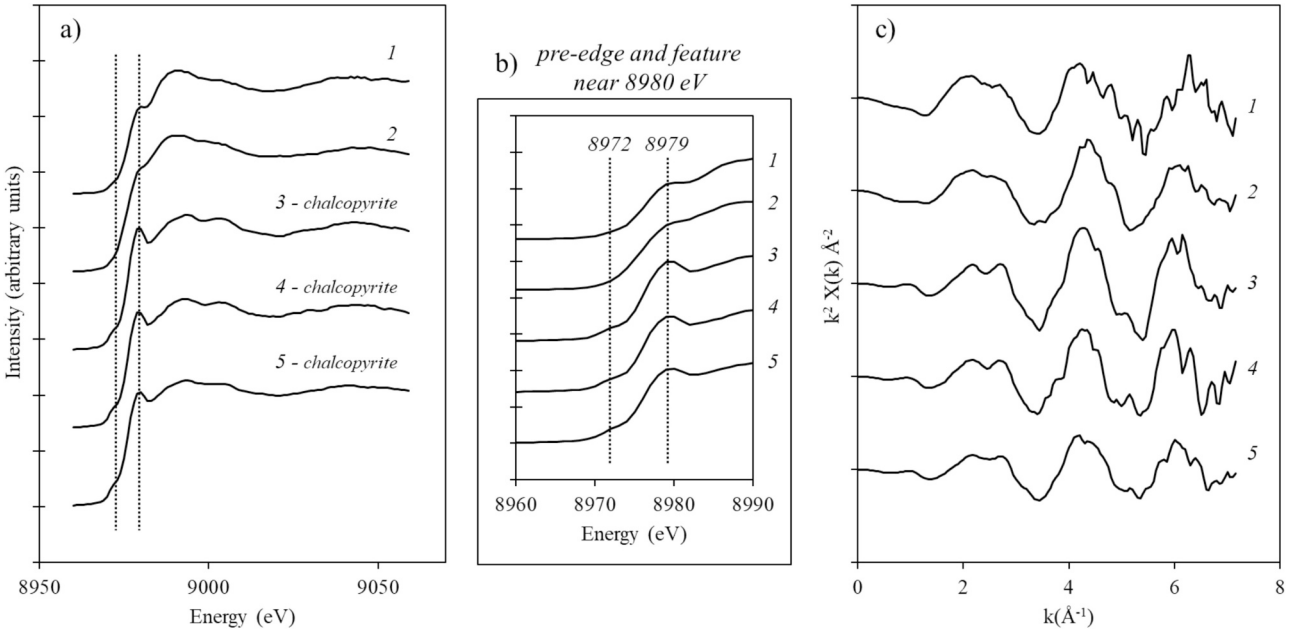

Fig. 9. a) and b) Examples of Cu K-edge μ-XANES spectra (from 1 to 5) obtained on the PUMA beamline at SOLEIL synchrotron facility for particles identified preliminary by μ-XRF mapping in layer ZH2 at 16–18 cm depth. Mineral phases are indicated for the one identified. The panel b) corresponds to a zoom on the pre-edge and features of Cu K-edge μ-XANES spectra between 8960 and 8990 eV.

derived sublayer (37%) than from the Rophin-derived sublayer (16%). BNL samples contained chalcopyrite crystals and low *POC*, while higher *POC* in Rophin samples could led to higher stability of Cu-POM species. Similarly, very low Cu contents were found for ZH1 and ZH3 samples (Fig. 6, Fig. S9). These results aligned with previous studies showing strong affinity for POM (Manceau and Matynia, 2010; Fulda et al., 2013), with Cu forming stable complexes due to its high charge/radius ratio (Covelo et al., 2007a, 2007b; Manceau and Matynia, 2010; Vega et al., 2006). Moreover, Cu association with clay minerals like vermiculite or smectite in mining deposits (their presence being confirmed by XRD) could not be excluded (Covelo et al., 2007a, 2007b; Manceau and Matynia, 2010; Vega et al., 2006).

In summary, in the BNL-originated deposit sub-layer, Cu speciation was broadly divided into easily and poorly extractable species, suggesting the coexistence of reactive and more stable Cu pools. The chemical treatment of BNL-ore, water table fluctuations and redox changes occurring in the wetland (Martin et al., 2020, 2021) could have caused partial oxidation of chalcopyrite, the main crystalline Cu mineral species identified in the BNL-originated deposit. The mechanical treatment of BNL ore along with episodic oxygen exposure during low-water periods and wet–dry cycling in the wetland can promote sulfide oxidation by increasing mineral surface reactivity and oxygen diffusion. This process may result in the release of Cu and Fe and the formation of more soluble species such as Cu adsorbed on mineral surfaces, Cu-sulfate, thus increasing Cu mobility. High Cu levels recorded in *POC*-rich layers (ZH1, ZH3) and the Rophin-derived sub-layer were in good agreement with vertical redistribution of easily extractable Cu from the BNL-originated mining deposits to the *POC*-rich layers.

3.4.4. Iron speciation in soil layers

In the wetland, Fe was mainly associated with refractory mineral phases (63–82% of total Fe) resistant to 1 mol.L^{-1} HCl, consistent with BCR F4 step results (34–79% of total Fe) targeting the residual fraction (Fig. 6). XRD and SEM analyses indicated Fe was mainly present as biotite and clay minerals (*e.g.*, vermiculite and illite), with minor contributions from refractory phases such as sulfide (pyrite, altered chalcopyrite), titanium oxide, or plumbogummite (Fig. S4-S6, Table S5-S6). The absence of Fe-sulfides after the BCR F3 step, in the BNL-derived sub-layer marked by chalcopyrite crystals, confirmed that these phases were digested with H_2O_2 (Fig. S6). In addition, 32–35% of total Fe were extracted during the BCR F2 step in ZH1 and ZH3 layers, suggesting a significant Fe oxyhydroxides fraction.

Total Fe contents were similar across the three layers (7000–8500 mg.kg^{-1}), except in the BNL-derived and mixing sublayers (ZH2), where low levels were found (4435 and 4687 mg.kg^{-1}; Fig. S9). These differences could be attributed to the presence of POC in ZH1, ZH3 layers and the Rophin-derived sub-layers (ZH2), which also led to higher extractable Fe amounts in the BCR F1-F3 steps, consistent with 1 mol.L^{-1} HCl and CBA extractions results (Fig. 6, Fig. S9). In addition, ZH2 sub-layers could contain less hematite – likely contributing to the BCR F2 step – as suggested in the detailed metallogenic study of the BNL ore (Cuney, 1978).

3.4.5. Overview of the elemental fractionation within the various soil layers

In conclusion, U, Cu, and Pb were largely present as low-extractable species bound to POM in POC-rich layers (ZH1 and ZH3), consistent with previous local studies (Martin et al., 2020, 2021; Grangeon et al., 2023; Geng et al., 2024). In contrast, in mining deposits derived from BNL and Rophin treatment ores (ZH2), these metals were mainly found associated with reducible Fe oxyhydroxides and clays. Metal speciation affects mobility and contamination potential of soils/groundwaters during hydrological events like floodings or droughts. Water table fluctuations and associated redox shifts could have driven vertical and/or lateral redistribution of metals from U-mining deposits to the *POC*-rich layers, likely through desorption and/or dissolution mechanisms of metal-bearing species (Stetten et al., 2018b; Sharma et al., 2022). Additionally, single-step and sequential chemical extractions from mining-impacted layers, supported with mineralogical data, revealed significant differences in the reactivity and extractability of adsorbed species (BCR F1 step) and in the diversity of metal-bearing crystalline phases.

To further explore these differences, normalized deionized water leaching tests were performed and discussed in the next section.

3.5. Metal leachability from the different soil layers

Natural wetlands are known to efficiently sequestrate uranium and

trace metals (Stetten et al., 2018b; Lefebvre et al., 2022; Wang et al., 2014; Lin et al., 2024; Li et al., 2014). Their high capacity for metals sequestration is largely attributed to the abundance of reactive Fe oxyhydroxides, clays minerals, and POM, which promote metal immobilization through adsorption, co-precipitation, complexation, and reductive transformation processes (Grybos et al., 2007; Stetten et al., 2018b; Lefebvre et al., 2022; Wang et al., 2014; Lin et al., 2024; Li et al., 2014; Owen and Otton, 1995; Schöner et al., 2009). In mining-impacted wetlands worldwide, Fe- and organic-rich soils and sediments have been shown to act as major repositories for metals transported from upstream mining areas, leading to substantial long-term accumulation within depositional zones (Sobolewski, 1999; Li et al., 2014; Wang et al., 2013; Stetten et al., 2018b). However, long-term metal retention in wetlands could be influenced by seasonal hydrological fluctuations and POM dynamics, which regulated redox conditions and metal speciation (Stetten et al., 2018b; Kaplan et al., 2017, 2024). Flooding events, commonly reported in both natural and mining-impacted wetlands, could induce sharp decreases in oxygen levels, promoting anaerobic bacterial activity and reductive dissolution of metal-bearing Fe(III) and Mn(III/IV) oxyhydroxides (Weber et al., 2009). Such redox-driven transformations may release previously immobilized U and trace metals into porewaters and potentially into overlying surface waters. In addition to redox processes, flood events can also enhance the physical mobilization of contaminants as particulate transport. The resuspension of fine particles and the transport of metal-bearing colloids can become a pathway for downstream export in wetland (Wang et al., 2013).

Dry events also influence metal redistribution in wetland systems. It could promote the oxidation of metal-bearing sulfides and other reduced forms in oxic condition during low-water stages, leading to the formation of secondary phases (Bostick et al., 2001; Hofmann and Schuwirth, 2008; Courtin-Nomade et al., 2009; Kimball et al., 2010). Similar oxidative transformations have been reported for reduced U-phases, including U(IV) phosphates, which may partially reoxidize under prolonged exposure to oxygen (Stetten et al., 2018b, 2020). However, already oxidized Cu—Pb phases in mining deposits (*e.g.,* plumbogummite, Cu sulfates) would be expected to be stable or evolved into more stable forms, supporting long-term Cu and Pb sequestration (Nriagu, 1974; Baker et al., 2014).

To access metal leachability, the normalized leaching test NF-EN 12457-2 (Kosson et al., 2002) was conducted. Dissolved metal concentrations and corresponding mass removals for ZH soil samples were determined in Table 2 and Fig. 10. No significant pH changes occurred during these tests (pH = 4.6–5.1). It should be noted that redox-sensitive elements like U could have changed during sampling and storage; therefore, results should be considered and interpreted under oxidizing conditions. Although the absence of porewater chemistry data limits direct assessment of U and associated metals mobilities under *in situ* conditions, previous studies report similar pH range as well as redox-sensitive fluctuations (Grangeon et al., 2023; Martin et al., 2020, 2021; Montavon et al., 2025), that are consistent with the solid-phase reactivity patterns observed in this work. Previous studies on the wetland soils with high-resolution pore-water profiles indicate that radium exhibits increasing ^{226}Ra concentrations with depth reflecting i) a downward migration of ^{226}Ra or ii) a K_d value much lower in a paleosoil region (Boudias et al., 2024).

Table 2
Fe, Cu, Pb and U concentration (mg.L^{-1}) extracted using the leaching procedure NF EN 12457-2 in each horizon of the soil core ZH; Relative Standard Deviations (%) are indicated under elements.

Soil core layer	Depth [cm]	Cu	Zn	U	Pb
		<1%	<1%	<1%	<5%
ZH1	1.5	0.106	0.113	0.235	0.193
	6.5	0.111	0.095	0.272	0.092
BNL impacted layer	9.0	0.160	0.062	0.290	0.088
	10.5	0.226	0.028	0.455	0.114
	12.5	3.165	0.527	3.475	1.378
Mining deposit mixing	15.0	0.274	0.143	1.853	0.847
	17.0	0.702	0.170	2.932	0.759
Rophin impacted layer	19.0	0.094	0.201	0.943	0.89
	21.0	0.090	0.337	0.393	0.461
ZH3	27.0	0.006	0.048	0.033	0.029
	41.0	0.001	0.017	0.042	0.239

The highest Cu, Pb and U concentrations were observed in leachates from the BNL-derived sublayer (located at 11–14 cm depth in Fig. 10), with values of 3165, 1378, and 3475 μg.L^{-1}, respectively. These yielded mass removal of 31.65, 13.78 and 34.75 mg.kg^{-1}, respectively. In contrast, the normalized deionized water extraction on the Rophin-derived sublayer (located at 18–20 cm depth in Fig. 10) showed lower Cu, Pb and U concentrations (90, 940, and 890 μg.L^{-1}, respectively) and mass removals (0.94, 8.90 and 9.43 mg.kg^{-1}, respectively).

Although the deionized water extraction does not reproduce the full chemical complexity of wetland porewaters. These results show that a small fraction of U remains exchangeable under near-natural conditions, while the majority of U is associated with less reactive phases. Consistently, Montavon et al. (2025) investigated mining materials collected from the same wetland, excluding the organic layers considered here, and showed that only a limited proportion of U (1–10%) behaves as a labile pool under near-natural conditions, characterized by relatively low $K_{d,labile}$ values (20–80 L·kg^{-1}), whereas most U remains inert. Within a mechanistic framework described in Coppin et al., 2023, and using the solid/liquid ratio defined by the NF EN 12457–2 standard for the normalized test in the present study, the average U concentrations extractable by deionized water were theoretically estimated for the following samples, based on the two methodologies reported by Montavon et al. (2025): AD-1,2,4: 2.9 mg.L^{-1}; E 0.2–0.6 mg.L^{-1}; F: 2.8–3.1 mg.L^{-1}; G: 1.1 mg.L^{-1}; and H: 4.2–5.1 mg.L^{-1}. All the values fall within the same range as those measured for mining materials in the present study (Table 2), supporting the consistency between both datasets. These findings suggest that the deionized water test effectively captures the readily exchangeable or weakly bound fraction of U in those samples (Montavon et al., 2025). These findings suggest that U lability in these soils is not directly proportional to total uranium content but rather controlled by the reactivity of surface-bound species and their response to redox and hydrological fluctuations, with implications for long-term U mobility under changing environmental conditions.

These results also highlighted distinct geochemical behaviors between the two U-mining materials, consistent with earlier mineralogical observations (Section 3.3). Long-term exposure to oxygen, combined with seasonal wet-dry cycles characteristic of the wetland, could promote sulfide oxidation and increase mineral surface area. It could promote the development of micro-fractures in sulfide (Liu et al., 2021), as well as facilitate oxygen diffusion and the concomitant release of trace metals from this mineral phase (Nordstrom, 2011). In BNL-derived materials, inherited primary ore minerals (if still present at the moment of the deposition in the wetland) such as pitchblende (UO_2) and chalcopyrite ($CuFeS_2$), are thermodynamically unstable under oxidizing conditions, promoting U(VI) release and sulfide oxidation, which in turn favors the formation of Fe-oxyhydroxides and secondary U phases (Steudel, 2020; Grenthe et al., 2011). Those could explain the persistence of a measurable available U and Cu fraction by the leaching test. The higher Cu and U extractability in the BNL-derived sublayer likely could reflect partial chalcopyrite dissolution and the presence of less stable sorbed U species (Section 3.4). concentrations and the absence of chalcopyrite crystals in the Rophin-derived sub-layer could explain its lower reactivity compared to the BNL-derived sub-layer.

Metal extractability was also higher for Pb in the BNL-derived sublayer (13.78 mg.kg^{-1} *vs* 8.90 mg.kg^{-1} for the Rophin-derived sub-layer), though less markedly than for Cu and U. A radiogenic Pb signature (^{206}Pb/^{207}Pb ≈ 1.8) in the leachate from this sublayer suggested redistribution of Pb isotopes from U-rich grains to more labile phases (*e.g.*, clays, Fe/Mn oxyhydroxides). Lower extraction capacity at 8–11 cm

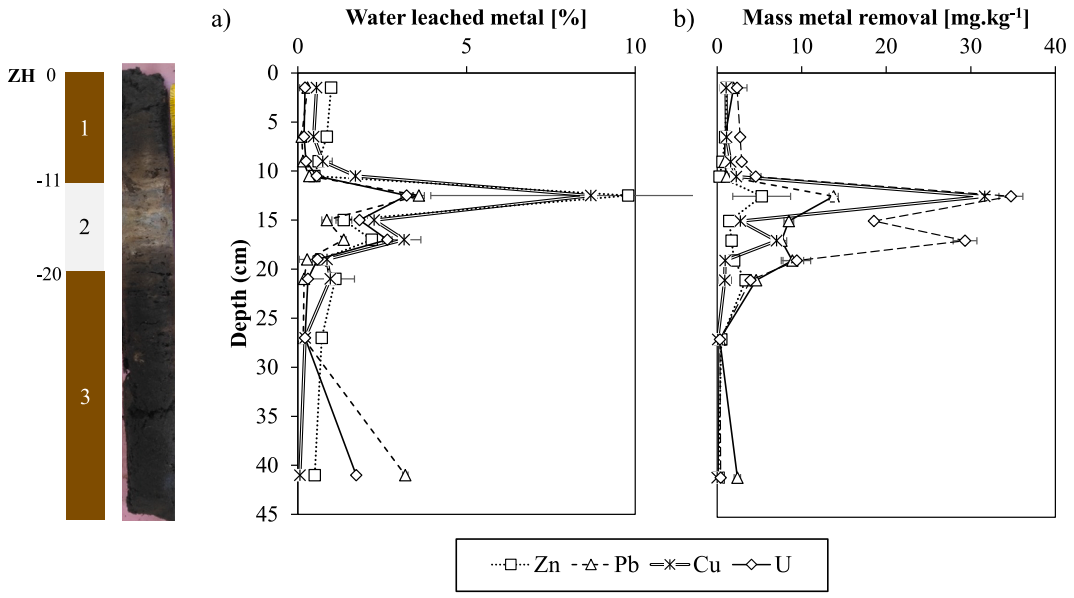

Fig. 10. Amounts of metals leached from the NF-EN-12457 leaching tests expressed in a) percentage of metal leached compared to the total elemental amount and b) in mass metal removal. The distinction of three well-defined geochemical layers within the "ZH" soil core was explained in Section 3.1.

depth could likely reflect reduced U oxide abundance and higher *POC* content.

The Rophin-derived sub-layer is characterized by a higher abundance of secondary U-bearing phases (*e.g.,* U adsorbed forms) and phosphate minerals (*e.g.,* plumbogummite), which are more stable under oxic conditions than sulfide assemblages. The solubility of the Rophin-primary ore phases indeed contributes to their contrasting behavior. For instance, parsonite dissolution can be expressed as:

$$Pb_2(UO_2)(PO_4)_2 \rightleftharpoons 2Pb^{2+} + UO_2{}^{2+} + 2PO_4{}^{3-} \quad (\log K_{sp} \approx -45.8) \tag{1}$$

Autunite dissolution as:

$$Ca(UO_2)_2(PO_4)_2{\cdot}3H_2O \rightleftharpoons Ca^{2+} + 2UO_2{}^{2+} + 2PO_4{}^{3-} + 3H_2O \quad (\log K_{sp} \approx -48.36) \tag{2}$$

and torbernite dissolution as:

$$Cu(UO_2)_2(PO_4)_2{\cdot}8H_2O \rightleftharpoons Cu^{2+} + 2UO_2{}^{2+} + 2PO_4{}^{3-} + 8H_2O \quad (\log K_{sp} \approx -41.0) \tag{3}$$

These logarithmic solubility product constants (log K_{sp}) indicate moderate thermodynamic stability compared to extremely insoluble Pb-phosphate phases such as plumbogummite:

$$PbAl_3(PO_4)_2(OH)_5{\cdot}H_2O \rightleftharpoons Pb^{2+} + 3Al^{3+} + 2PO_4{}^{3-} + 5OH^- + H_2O \quad (\log K_{sp} \approx -99.3) \tag{4}$$

and pyromorphite (Gorman-Lewis et al., 2009; Nriagu, 1974):

$$Pb_5(PO_4)_3Cl \rightleftharpoons 5Pb^{2+} + 3PO_4{}^{3-} + Cl^- \quad (\log K_{sp} \approx -84.4) \tag{5}$$

This could account for the limited occurrence of parsonsite and torbernite minerals in the analyzed samples. While plumbogummite and pyromorphite are typically secondary phases that may form following the dissolution and redistribution of these primary Pb- and U-bearing minerals (Nriagu, 1974), contributing to long-term Pb immobilization in weathered environments.

These mineralogical differences between BNL and Rophin derived sub-layers lead to distinct long-term leaching behaviors, with Rophin-derived deposits showing greater resistance to oxidative remobilization.

In addition to mineralogical influence, POM plays a key role in stabilizing U in Rophin-derived deposits (Section 3.4.1), through complexation with organic ligands, limiting its immediate availability for desorption with deionized water. Such associations are consistent with the lower labile fractions measured in this sub-layer and highlight the importance of organic-rich matrices influencing metal mobility.

Overall, the contrasted behavior of BNL- and Rophin-derived sub-layers highlights the influence of source mineralogy on long-term contaminant dynamics. Sulfide-rich deposits promote metal release under oxic and fluctuating hydrological conditions, whereas phosphate- and organic-rich materials favor U retention. These findings demonstrate that U mobility in mining-impacted wetlands cannot be exclusively predicted from present-day environmental conditions but must also account for the mineralogical inheritance of ore processing.

Leached Cu, Zn and Pb contents from the ZH soil core were below the European regulatory threshold values for non-hazardous waste (Table S10), indicating limited metal mobility from the wetland.

The study highlighted that uranium initially hosted in primary U-bearing minerals was released during alteration and subsequently sequestered into secondary bearing-phases such as Fe oxyhydroxides, clays, and organo-metallic associations, underscoring the role of post-depositional processes in governing U and metal speciation and mobility in wetland soils. This behavior is consistent with results obtain by Montavon et al. (2025) on samples kept under anoxic conditions from the same wetland. With U being predominantly retained as surface-bound species, likely U(VI) adsorbed onto clay minerals and Fe–organic aggregates, while a significant proportion of adsorbed U exhibits desorption hysteresis and behaves operationally as inert (Montavon et al., 2025). The consistency between our findings and those reported for mining-impacted wetlands underscores the key processes on metal mobility, such as the dominant control of redox oscillations, OM, and mineralogical inheritance. The detailed characterization of contaminant-hosting phases and their reactivity offered key input data for predictive geochemical and transport models for evaluating the long-term fate of mining-influenced sites.

4. Conclusion

This study confirmed that the downstream wetland at the former Rophin U mining site (France) was influenced by mining deposit sources

from the former processing of BNL (pitchblende) and Rophin (parsonsite) ores. Regarding the origin of metals, the combination of U mineralogy and stable Pb isotopic data allowed the identification of BNL and Rophin ore-derived deposits as the primary sources of U, Pb, and Cu in the wetland sediments, clearly linking historical mining activities to downstream metal accumulation. According to the combination of mineralogical, speciation and chemical extraction data, this work highlighted the significant redistribution of U and associated minerals from primary ore minerals to secondary phases, affecting their mobility and long-term stability with time and depth during pedogenesis processes. The main metal-bearing phases identified included Fe oxyhydroxides, clay minerals, and to a lesser extent, particulate organic matter. In addition, metals were also hosted by rarer phases, such as U oxides, phosphates like plumbogummite, Ti oxides, Cu and Pb sulfides and sulfates. The reactivity of metal-bearing phases showed that metals were over twice as extractable from BNL compared to the ones from Rophin source. In contrast, minimal extraction for Cu, Pb, Zn and U from the organic-rich surface soils confirmed the strong metal-binding capacity of natural organic matter in wetland system, thus limiting their mobility. Although microbial processes were not directly investigated in this study, they are likely to contribute to Cu, Fe and U redox cycling in the wetland. Iron- and sulfate-reducing microorganisms may indirectly influence redox sensitive elements (*e.g.,* U, Fe, Mn) speciation by modifying the redox state and/or crystallinity of Fe-bearing phases (Chang et al., 2014; Kaplan et al., 2024; Wang et al., 2014; Bargar et al., 2008). The present study thus establishes a geochemical framework within which biologically mediated processes may occur. These findings help to improve our understanding of U and associated metals fate in historically contaminated wetlands and the ability of such systems to accommodate anthropogenic deep modifications. All this information could be helpful for improving geochemical transport models able to predict the fate of metals in wetlands.

CRediT authorship contribution statement

Louise Darricau: Writing – review & editing, Writing – original draft, Validation, Resources, Investigation. **Alexandra Courtin:** Writing – review & editing, Writing – original draft, Validation, Supervision, Project administration, Investigation, Conceptualization. **Josselin Gorny:** Writing – review & editing, Writing – original draft, Validation, Supervision, Investigation, Conceptualization. **Alkiviadis Gourgiotis:** Writing – review & editing, Validation. **David Suhard:** Investigation. **Emmanuel Joussein:** Investigation. **Solenn Réguer:** Investigation. **Sebastian Schöder:** Investigation. **Julia Cucinotta:** Investigation. **Pascale Blanchart:** Investigation, Conceptualization. **Mathilde Zebracki:** Investigation, Conceptualization. **Arnaud Mangeret:** Writing – review & editing, Writing – original draft, Validation, Supervision, Project administration, Conceptualization.

Declaration of competing interest

The authors declare that they have no known competing financial interests or personal relationships that could have appeared to influence the work reported in this paper.

Acknowledgments

The experiments were performed at the LUTECE platform (an ASNR experimental platform). This is PATERSON, the ASNR's mass spectrometry platform, contribution n°27 (DOI: 10.57876/8HJP-4744). Aurélie Lambert is also acknowledged for soil core sampling assistance. We thank Olivier Diez, Cyrielle Jardin, and Gilles Alcalde from LUTECE (IRSN), Serge Miska and Julius Nouet from GEOPS and Michel Fialin and Nicolas Rividi from Camparis for their help in chemical, mineralogical (SEM and XRD) and EPMA analyses respectively. We acknowledge SOLEIL for provision of synchrotron radiation beamtime and thank the staff of the PUMA and Diffabs beamline for their assistance in the measurement of μXRF and Cu-K-edge and Pb-L^{III}-edge μXANES (Proposals No. 20220477 and No. 20220396, respectively). This work was supported by ASNR.

Appendix A. Supplementary data

Supplementary data to this article can be found online at https://doi.org/10.1016/j.chemgeo.2026.123332.

Data availability

Data will be made available on request.

References

Aamrani, S.E., Giménez, J., Rovira, M., Seco, F., Grivé, M., Bruno, J., Duro, L., de Pablo, J., 2007. A spectroscopic study of uranium(VI) interaction with magnetite. Appl. Surf. Sci. 253, 8794–8797. https://doi.org/10.1016/j.apsusc.2007.04.076.

Alessi, D.S., Uster, B., Veeramani, H., Suvorova, E.I., Lezama-Pacheco, J.S., Stubbs, J.E., Bargar, J.R., Bernier-Latmani, R., 2012. Quantitative separation of monomeric U(IV) from UO_2 in products of U(VI) reduction. Environ. Sci. Technol. 46, 6150–6157. https://doi.org/10.1021/es204123z.

Audry, S., Grosbois, C., Bril, H., Schäfer, J., Kierczak, J., Blanc, G., 2010. Post-depositional redistribution of trace metals in reservoir sediments of a mining/smelting-impacted watershed (the Lot River, SW France). Appl. Geochem. 25, 778–794. https://doi.org/10.1016/j.apgeochem.2010.02.009.

Avasarala, S., Lichtner, P.C., Ali, A.-M.S., González-Pinzón, R., Blake, J.M., Cerrato, J.M., 2017. Reactive transport of U and V from abandoned uranium mine wastes. Environ. Sci. Technol. 51, 12385–12393. https://doi.org/10.1021/acs.est.7b03823.

Bacon, Jeffrey R., Davidson, M.C., 2008. Is there a future for sequential chemical extraction? Analyst 133, 25–46. https://doi.org/10.1039/B711896A.

Baker, L.C., Pierzynski, G.M., Hettiarachchi, G.M., Scheckel, K.G., Newville, M., 2014. Micro-X-ray fluorescence, micro-X-ray absorption spectroscopy, and micro-X-ray diffraction investigation of lead speciation after the addition of different phosphorus amendments to a smelter-contaminated soil. J. Environ. Qual. 43. https://doi.org/10.2134/jeq2013.07.0281.

Bargar, J.R., Bernier-Latmani, R., Giammar, D.E., Tebo, B.M., 2008. Biogenic uraninite nanoparticles and their importance for uranium remediation. Elements 4, 407–412. https://doi.org/10.2113/gselements.4.6.407.

Bartl, U., Czurda, K.A., 1991. Migration and retention phenomena of radionuclides in clay-barrier systems. Appl. Clay Sci. 6, 195–214. https://doi.org/10.1016/0169-1317(91)90025-5.

Behrends, T., Van Cappellen, P., 2005. Competition between enzymatic and abiotic reduction of uranium(VI) under iron reducing conditions. Chem. Geol. 220, 315–327. https://doi.org/10.1016/j.chemgeo.2005.04.007.

Blake, J.M., Avasarala, S., Artyushkova, K., Ali, A.-M.S., Brearley, A.J., Shuey, C., Robinson, Wm.P., Nez, C., Bill, S., Lewis, J., Hirani, C., Pacheco, J.S.L., Cerrato, J.M., 2015. Elevated concentrations of U and co-occurring metals in abandoned mine wastes in a Northeastern arizona native American community. Environ. Sci. Technol. 49, 8506–8514. https://doi.org/10.1021/acs.est.5b01408.

Bostick, B.C., Hansel, C.M., Fendorf, S., 2001. Seasonal fluctuations in zinc speciation within a contaminated wetland. Environ. Sci. Technol. 35, 3823–3829. https://doi.org/10.1021/es010549d.

Boudias, M., Nivesse, A.-L., Gorny, J., Quémet, A., Delaunay, N., Montavon, G., Landesman, C., Gourgiotis, A., 2024. Microvolume analysis of 226Ra by inductively coupled plasma mass spectrometry: environmental applications to high-resolution profile of wetland soil pore waters. Microchem. J. 204, 110971. https://doi.org/10.1016/j.microc.2024.110971.

Cappuyns, V., Swennen, R., Niclaes, M., 2007. Application of the BCR sequential extraction scheme to dredged pond sediments contaminated by Pb–Zn mining: a combined geochemical and mineralogical approach. J. Geochem. Explor. 93, 78–90. https://doi.org/10.1016/j.gexplo.2006.10.001.

Cardoso Fonseca, E., Martin, H., 1986. The selective extraction of Pb and Zn in selected mineral and soil samples, application in geochemical exploration (Portugal). J. Geochem. Explor. 26, 231–248. https://doi.org/10.1016/0375-6742(86)90074-9.

Cervi, E.C., Clark, S., Boye, K.E., Gustafsson, J.P., Baken, S., Burton, G.A., 2021. Copper transformation, speciation, and detoxification in anoxic and suboxic freshwater sediments. Chemosphere 282, 131063. https://doi.org/10.1016/j.chemosphere.2021.131063.

Chang, H., Buettner, S.W., Seaman, John.C., Jaffé, P.R., Koster van Groos, Paul.G., Li, D., Peacock, A.D., Scheckel, K.G., Kaplan, D.I., 2014. Uranium immobilization in an Iron-Rich Rhizosphere of a native wetland plant from the savannah river site under reducing conditions. Environ. Sci. Technol. 48, 9270–9278. https://doi.org/10.1021/es5015136.

Chang, C.-Y., Wang, C.-F., Mui, D.T., Chiang, H.-L., 2009. Application of methods (sequential extraction procedures and high-pressure digestion method) to fly ash particles to determine the element constituents: a case study for BCR 176. J. Hazard. Mater. 163, 578–587. https://doi.org/10.1016/j.jhazmat.2008.07.039.

Chautard, C., Beaucaire, C., Gerard, M., Roy, R., Savoye, S., Descostes, M., 2020. Geochemical characterization of uranium mill tailings (Bois Noirs Limouzat, France)

highlighting the U and 226Ra retention. J. Environ. Radioact. 218, 106251. https://doi.org/10.1016/j.jenvrad.2020.106251.
Chen, N., Jiang, D.T., Cutler, J., Kotzer, T., Jia, Y.F., Demopoulos, G.P., Rowson, J.W., 2009. Structural characterization of poorly-crystalline scorodite, iron(III)-arsenate coprecipitates and uranium mill neutralized raffinate solids using X-ray absorption fine structure spectroscopy. Geochim. Cosmochim. Acta 73, 3260–3276. https://doi.org/10.1016/j.gca.2009.02.019.
Cooper, D.C., Morse, J.W., 1998. Extractability of metal sulfide minerals in acidic solutions: application to environmental studies of trace metal contamination with anoxic sediments. Environ. Sci. Technol. 32, 1076–1078. https://doi.org/10.1021/es970415t.
Coppin, F., Février, L., Martin-Garin, A., 2023. Operational method to easily determine the available fraction of a contaminant in soil and the associated soil-solution distribution coefficient. ACS Earth Space Chem. 7, 559–570. https://doi.org/10.1021/acsearthspacechem.2c00324.
Corkhill, C.L., Crean, D.E., Bailey, D.J., Makepeace, C., Stennett, M.C., Tappero, R., Grolimund, D., Hyatt, N.C., 2017. Multi-scale investigation of uranium attenuation by arsenic at an abandoned uranium mine, South Terras. Npj Mater. Degrad. 1, 19. https://doi.org/10.1038/s41529-017-0019-9.
Courtin-Nomade, A., Grosbois, C., Marcus, M.A., Fakra, S.C., Beny, J.-M., Foster, A.L., 2009. The weathering of a sulfide orebody: speciation and fate of some potential contaminants. Can. Mineral. 47, 493–508. https://doi.org/10.3749/canmin.47.3.493.
Courtin-Nomade, A., Waltzing, T., Evrard, C., Soubrand, M., Lenain, J.-F., Ducloux, E., Ghorbel, S., Grosbois, C., Bril, H., 2016. Arsenic and lead mobility: from tailing materials to the aqueous compartment. Appl. Geochem. https://doi.org/10.1016/j.apgeochem.2015.11.002.
Covelo, E.F., Vega, F.A., Andrade, M.L., 2007a. Competitive sorption and desorption of heavy metals by individual soil components. J. Hazard. Mater. 140, 308–315. https://doi.org/10.1016/j.jhazmat.2006.09.018.
Covelo, E.F., Vega, F.A., Andrade, M.L., 2007b. Simultaneous sorption and desorption of Cd, Cr, Cu, Ni, Pb, and Zn in acid soils: II. Soil ranking and influence of soil characteristics. J. Hazard. Mater. 147, 862–870. https://doi.org/10.1016/j.jhazmat.2007.01.123.
Cumberland, S.A., Etschmann, B., Brugger, J., Douglas, G., Evans, K., Fisher, L., Kappen, P., Moreau, J.W., 2018. Characterization of uranium redox state in organic-rich Eocene sediments. Chemosphere 194, 602–613. https://doi.org/10.1016/j.chemosphere.2017.12.012.
Cumming, G.L., Richards, J.R., 1975. Ore lead isotope ratios in a continuously changing earth. Earth Planet. Sci. Lett. 28, 155–171. https://doi.org/10.1016/0012-821X(75)90223-X.
Cuney, M., 1978. Geologic environment, mineralogy, and fluid inclusions of the Bois-Noirs-Limouzat uranium vein, Forez, France. Econ. Geol. 73, 1567–1610. https://doi.org/10.2113/gsecongeo.73.8.1567.
Cuvier, A., Pourcelot, L., Probst, A., Prunier, J., Le Roux, G., 2016. Trace elements and Pb isotopes in soils and sediments impacted by uranium mining. Sci. Total Environ. 566–567, 238–249. https://doi.org/10.1016/j.scitotenv.2016.04.213.
Darricau, L., Mangeret, A., Gorny, J., Joussein, E., Schoeder, S., Reyss, J.-L., Thouvenot, A., Courtin, A., 2024. Evaluation of the speciation and availability of Cu, Sn, Bi and U from lacustrine sediments influenced by former mining activities. Appl. Geochem. 167, 105995. https://doi.org/10.1016/j.apgeochem.2024.105995.
Davey, P.T., Scott, T.R., 1956. Adsorption of uranium on clay minerals. Nature 178. https://doi.org/10.1038/1781195a0, 1195–1195.
de Matos, A.T., Fontes, M.P.F., da Costa, L.M., Martinez, M.A., 2001. Mobility of heavy metals as related to soil chemical and mineralogical characteristics of Brazilian soils. Environ. Pollut. 111, 429–435. https://doi.org/10.1016/S0269-7491(00)00088-9.
Dewey, C., Bargar, J.R., Fendorf, S., 2021. Porewater lead concentrations limited by particulate organic matter coupled with ephemeral iron(III) and sulfide phases during redox cycles within contaminated floodplain soils. Environ. Sci. Technol. 55, 5878–5886. https://doi.org/10.1021/acs.est.0c08162.
Donahue, R., Hendry, M.J., Landine, P., 2000. Distribution of arsenic and nickel in uranium mill tailings, Rabbit Lake, Saskatchewan, Canada. Appl. Geochem. 15, 1097–1119. https://doi.org/10.1016/S0883-2927(99)00114-6.
Doughman, M.S., O'Shea, K.E., Qafoku, N.P., Emerson, H.P., Szecsody, J.E., Carroll, K.C., Katsenovich, Y.P., 2024. Impact of chromium (VI) as a co-contaminant on the sorption and co-precipitation of uranium (VI) in sediments under mildly alkaline oxic conditions. J. Environ. Manage. 349, 119463. https://doi.org/10.1016/j.jenvman.2023.119463.
Ecce Terra, 2018. PLATEFORME MEN / CAMPARIS [WWW Document]. Obs. Sci. Univers UPMC-INSU. URL http://ecceterra.sorbonne-universite.fr/fr/les_services_aoc/les_plateformes_analytiques2/plateforme_men.html (accessed 2.16.23).
England, K.E.R., Charnock, J.M., Pattrick, R.A.D., Vaughan, D.J., 1999. Surface oxidation studies of chalcopyrite and pyrite by glancing-angle X-ray absorption spectroscopy (REFLEXAFS). Mineral. Mag. 63, 559–566. https://doi.org/10.1180/002646199548718.
Essilfie-Dughan, J., Pickering, I.J., Hendry, M.J., George, G.N., Kotzer, T., 2011. Molybdenum speciation in uranium mill tailings using X-ray absorption spectroscopy. Environ. Sci. Technol. 45, 455–460. https://doi.org/10.1021/es102954b.
Fanfani, L., Zuddas, P., Chessa, A., 1997. Heavy metals speciation analysis as a tool for studying mine tailings weathering. J. Geochem. Explor. 58, 241–248. https://doi.org/10.1016/S0375-6742(96)00059-3.
Feng, Y., Liu, P., Xie, X., Gan, Y., Su, C., Liu, Y., Finfrock, Y.Z., Wang, Y., 2022. Effect of oxidation on the release of multiple metals from industrially polluted sediments and synchrotron-based evidence of Cu-S dynamic association. J. Soil. Sediment. 22, 2827–2839. https://doi.org/10.1007/s11368-022-03288-8.
Ferrari, C., Resongles, E., Freydier, R., Casiot, C., 2021. A single-step purification method for the precise determination of the antimony isotopic composition of environmental, geological and biological samples by HG-MC-ICP-MS. J. Anal. At. Spectrom. 36, 776–785. https://doi.org/10.1039/D0JA00452A.
Foucault, Y., Schreck, E., Levêque, T., Pradère, P., Dumat, C., 2012. Vers une gestion raisonnée des terres excavées contaminées par des éléments traces métalliques (ETM). Environ. Risques Santé 11, 61–66. https://doi.org/10.1684/ers.2011.0506.
Fredrickson, J.K., Zachara, J.M., Kennedy, D.W., Duff, M.C., Gorby, Y.A., Li, S.W., Krupka, K.M., 2000. Reduction of U(VI) in goethite (α-FeOOH) suspensions by a dissimilatory metal-reducing bacterium. Geochim. Cosmochim. Acta 64, 3085–3098. https://doi.org/10.1016/S0016-7037(00)00397-5.
Fulda, B., Voegelin, A., Maurer, F., Christl, I., Kretzschmar, R., 2013. Copper redox transformation and complexation by reduced and oxidized soil humic acid. 1. X-ray absorption spectroscopy study. Environ. Sci. Technol. 47, 10903–10911. https://doi.org/10.1021/es4024089.
Geffroy, J., Sarcia, J.A., 1955. Contribution à l'étude des pechblendes françaises. Rapport CEA n°380.
Geng, T., Mangeret, A., Péron, O., Suhard, D., Gorny, J., Darricau, L., Le Coz, M., Ait-Ouabbas, N., David, K., Debayle, C., Blanchart, P., Montavon, G., Gourgiotis, A., 2024. Unveiling the origins and transport processes of radioactive pollutants downstream from a former U-mine site using isotopic tracers and U-238 series disequilibrium. J. Hazard. Mater. 472, 134416.
Gieré, R., Sidenko, N.V., Lazareva, E.V., 2003. The role of secondary minerals in controlling the migration of arsenic and metals from high-sulfide wastes (Berikul gold mine, Siberia). Appl. Geochem. 18, 1347–1359. https://doi.org/10.1016/S0883-2927(03)00055-6.
Gilson, E.R., Huang, S., Koster van Groos, P.G., Scheckel, K.G., Qafoku, O., Peacock, A.D., Kaplan, D.I., Jaffé, P.R., 2015. Uranium redistribution due to water table fluctuations in sandy wetland mesocosms. Environ. Sci. Technol. 49, 12214–12222. https://doi.org/10.1021/acs.est.5b02957.
Gorman-Lewis, D., Shvareva, T., Kubatko, K.-A., Burns, P.C., Wellman, D.M., McNamara, B., Szymanowski, J.E.S., Navrotsky, A., Fein, J.B., 2009. Thermodynamic properties of autunite, uranyl hydrogen phosphate, and uranyl orthophosphate from solubility and calorimetric measurements. Environ. Sci. Technol. 43, 7416–7422. https://doi.org/10.1021/es9012933.
Govinoaraju, K., De La Roche, H., 1977. Rapport (1966-1976) sur les éléments en traces dans trois roches standards géochimiques du CRPG. Basalte BR et Granites, GA et GH. Geostand. Newslett. 1, 67–100. https://doi.org/10.1111/j.1751-908X.1977.tb00860.x.
Grangeon, S., Roux, C., Lerouge, C., Chardon, P., Beuzeval, R., Montavon, G., Claret, F., Grangeon, T., 2023. Geochemical and mineralogical characterization of streams and wetlands downstream of a former uranium mine (Rophin, France). Appl. Geochem. 150, 105586. https://doi.org/10.1016/j.apgeochem.2023.105586.
Grenthe, I., Dro.zd.zy'nski, J., Fujino, T., Buck, E., Albrecht-Schmitt, T., Wolf, S., 2011. Uranium. Chem. Actin. Trans. Elem. 253–698.
Grybos, M., Davranche, M., Gruau, G., Petitjean, P., 2007. Is trace metal release in wetland soils controlled by organic matter mobility or Fe-oxyhydroxides reduction? J. Colloid Interface Sci. 314, 490–501. https://doi.org/10.1016/j.jcis.2007.04.062.
Gu, C., Anderson, W., Maggi, F., 2012. Riparian biogeochemical hot moments induced by stream fluctuations. Water Resour. Res. 48, W09546. https://doi.org/10.1029/2011WR011720.
Guiolliard, P.-C., 2002. L'uranium du Morvan et du Forez. Pierre-Christian Guiollard.
Haese, R.R., Schramm, J., Rutgers van der Loeff, M.M., Schulz, H.D., 2000. A comparative study of iron and manganese diagenesis in continental slope and deep sea basin sediments off Uruguay (SW Atlantic). Int. J. Earth Sci. 88, 619–629. https://doi.org/10.1007/s005310050292.
Heron, G., Crouzet, C., Bourg, A.C.M., Christensen, T.H., 1994. Speciation of Fe(II) and Fe(III) in contaminated aquifer sediments using chemical extraction techniques. Environ. Sci. Technol. 28, 1698–1705. https://doi.org/10.1021/es00058a023.
Himeur, N., Andres, C., 2012. Suivi environnemental du site de Rophin – Communes de Lachaux et Ris.
Hofmann, T., Schuwirth, N., 2008. Zn and Pb release of sphalerite (ZnS)-bearing mine waste tailings. J. Soil. Sediment. 8, 433–441. https://doi.org/10.1007/s11368-008-0052-y.
Hyacinthe, C., Van Cappellen, P., 2004. An authigenic iron phosphate phase in estuarine sediments: composition, formation and chemical reactivity. Mar. Chem. 91, 227–251. https://doi.org/10.1016/j.marchem.2004.04.006.
Hyacinthe, C., Bonneville, S., Van Cappellen, P., 2006. Reactive iron(III) in sediments: chemical versus microbial extractions. Geochim. Cosmochim. Acta 70, 4166–4180. https://doi.org/10.1016/j.gca.2006.05.018.
IRSN, 2024. MIMAUSA. website accessed March 25, 2024. https://mimausabdd.irsn.fr.
Kaplan, D.I., Buettner, S.W., Li, D., Huang, S., Koster van Groos, P.G., Jaffé, P.R., Seaman, J.C., 2017. In situ porewater uranium concentrations in a contaminated wetland: effect of seasons and sediment depth. Appl. Geochem. 85, 128–136. https://doi.org/10.1016/j.apgeochem.2016.11.017.
Kaplan, D.I., Boyanov, M.I., Losey, N.A., Lin, P., Xu, C., O'Loughlin, E.J., Santschi, P.H., Xing, W., Kuhne, W.W., Kemner, K.M., 2024. Uranium biogeochemistry in the rhizosphere of a contaminated wetland. Environ. Sci. Technol. 58, 6381–6390. https://doi.org/10.1021/acs.est.3c10481.
Kimball, B.E., Rimstidt, J.D., Brantley, S.L., 2010. Chalcopyrite dissolution rate laws. Appl. Geochem. 25, 972–983. https://doi.org/10.1016/j.apgeochem.2010.03.010.
Kosson, D.S., van der Sloot, H.A., Sanchez, F., Garrabrants, A.C., 2002. An integrated framework for evaluating leaching in waste management and utilization of secondary materials. Environ. Engin. Sci. 19, 159–204. https://doi.org/10.1089/109287502760079188.

Langmuir, D., 1978. Uranium solution-mineral equilibria at low temperatures with applications to sedimentary ore deposits. Geochim. Cosmochim. Acta 42, 547–569. https://doi.org/10.1016/0016-7037(78)90001-7.

Larner, B.L., Seen, A.J., Toxnsend, A.T., 2006. Comparative study of optimized BCR sequential extraction scheme and acid leaching of elements in the certified reference materials NIST 2711. Anal. Chim. Acta 556, 444–449. https://doi.org/10.1016/j.aca.2005.09.058.

Leclercq, N., Berthault, J., Le Langlois, F., Poirier, S., Bisou, J., Blache, F., Medjoubi, K., Mocuta, C., 2015. Flyscan: a fast and multi-technique data acquisition platform for the SOLEIL beamlines. In: *ICALEPCS 2015, the 15th International Conference on Accelerator and Large Experimental Control Systems*, 17–23 October 2015, Melbourne, Australia, Abstract No. WEPGF056 (2015).

Lefebvre, P., Le Pape, P., Mangeret, A., Gourgiotis, A., Sabatier, P., Louvat, P., Diez, O., Mathon, O., Hunault, M.O.J.Y., Baya, C., Darricau, L., Cazala, C., Bargar, J.R., Gaillardet, J., Morin, G., 2022. Uranium sorption to organic matter and long-term accumulation in a pristine alpine wetland. Geochim. Cosmochim. Acta 338, 322–346. https://doi.org/10.1016/j.gca.2022.10.018.

Leleyter, L., Rousseau, C., Biree, L., Baraud, F., 2012. Comparison of EDTA, HCl and sequential extraction procedures for selected metals (Cu, Mn, Pb, Zn) in soils, riverine and marine sediments. J. Geochem. Explor. 116-117, 51–59. https://doi.org/10.1016/j.gexplo.2012.03.006.

Li, D., Seaman, J.C., Chang, H.-S., Jaffe, P.R., Koster van Groos, P., Jiang, D.-T., Chen, N., Lin, J., Arthur, Z., Pan, Y., Scheckel, K.G., Newville, M., Lanzirotti, A., Kaplan, D.I., 2014. Retention and chemical speciation of uranium in an oxidized wetland sediment from the Savannah River Site. J. Environ. Radioact. 131, 40–46. https://doi.org/10.1016/j.jenvrad.2013.10.017. SPECIAL ISSUE: Environmental Radioactivity: Legacy Sites, Chernobyl and Fukushima; selected papers from the 12th International Conference on the Biogeochemistry of Trace Elements (ICOBTE).

Liger, E., Charlet, L., Van Cappellen, P., 1999. Surface catalysis of uranium(VI) reduction by iron(II). Geochim. Cosmochim. Acta 63, 2939–2955. https://doi.org/10.1016/S0016-7037(99)00265-3.

Lin, P., Boyanov, M.I., O'Loughlin, E.J., Xing, W., Kemner, K.M., Seaman, J., Simner, S. P., Kaplan, D.I., 2024. Uranium and nickel partitioning in a contaminated riparian wetland. Water 16, 966. https://doi.org/10.3390/w16070966.

Liu, H.-C., Nie, Z.-Y., Xia, J.-L., Zhu, H., Yang, Y., Zhao, C., Zheng, L., Zhao, Y.-D., 2015. Investigation of copper, iron and sulfur speciation during bioleaching of chalcopyrite by moderate thermophile Sulfobacillus thermosulfidooxidans. Int. J. Miner. Process. 137, 1–8. https://doi.org/10.1016/j.minpro.2015.02.008.

Liu, D., Zhang, G., Liu, J., Pan, G., Chen, Y., Wang, M., 2021. Studies on the surface oxidation and its role in the flotation of mixed Cu-Ni sulfide ore. Powder Technol. 381, 576–584. https://doi.org/10.1016/j.powtec.2020.12.038.

Macías, F., Pérez-López, R., Caraballo, M.A., Cánovas, C.R., Nieto, J.M., 2017. Management strategies and valorization for waste sludge from active treatment of extremely metal-polluted acid mine drainage: a contribution for sustainable mining. J. Clean. Prod. 141, 1057–1066. https://doi.org/10.1016/j.jclepro.2016.09.181.

Manceau, A., Matynia, A., 2010. The nature of Cu bonding to natural organic matter. Geochim. Cosmochim. Acta 74, 2556–2580. https://doi.org/10.1016/j.gca.2010.01.027.

Martin, A., Hassan-Loni, Y., Fichtner, A., Péron, O., David, K., Chardon, P., Larrue, S., Gourgiotis, A., Sachs, S., Arnold, T., Grambow, B., Stumpf, T., Montavon, G., 2020. An integrated approach combining soil profile, records and tree ring analysis to identify the origin of environmental contamination in a former uranium mine (Rophin, France). Sci. Total Environ. 747, 141295. https://doi.org/10.1016/j.scitotenv.2020.141295.

Martin, A., Montavon, G., Landesman, C., 2021. A combined DGT – DET approach for an in situ investigation of uranium resupply from large soil profiles in a wetland impacted by former mining activities. Chemosphere 279, 130526. https://doi.org/10.1016/j.chemosphere.2021.130526.

Mikhlin, Y.L., Likhatski, M.N., Bayukov, O.A., Knyazev, Y., Velikanov, D.A., Tomashevich, Y.V., Romanchenko, A.S., Vorobyev, S.A., Volochazev, M.V., Zharkov, S.M., Meira, D.M., 2021. Valleriite, a natural two-dimensional composite: X-ray absorption, photoelectron, and Mössbauer spectroscopy, and magnetic characterization. ACS Omega 6, 7533–7543. https://doi.org/10.1021/acsomega.0c06052.

Mikutta, C., Langner, P., Bargar, J.R., Kretzschmar, R., 2016. Tetra- and hexavalent uranium forms bidentate-mononuclear complexes with particulate organic matter in a naturally uranium-enriched peatland. Environ. Sci. Technol. 50, 10465–10475. https://doi.org/10.1021/acs.est.6b03688.

Monneron–Gyurits, M., Soubrand, M., Joussein, E., Courtin-Nomade, A., Jubany, I., Casas, S., Bahí, N., Faz, A., Gabarrón, M., Acosta, J.A., Martínez-Martínez, S., 2020. Investigating the relationship between speciation and oral/lung bioaccessibility of a highly contaminated tailing: contribution in health risk assessment. Environ. Sci. Pollut. Res. 27, 40732–40748. https://doi.org/10.1007/s11356-020-10074-x.

Montavon, G., Nivesse, A.-L., Martin, A., Arnold, T., Sachs, S., Bok, F., Scheinost, A.C., Stumpf, T., Coppin, F., Gourgiotis, A., Del Nero, M., Chardon, P., Landesman, C., 2025. Lability of uranium in a mine-impacted wetland 70 years after the contamination. Environ. Sci. Technol. 59, 26661–26671. https://doi.org/10.1021/acs.est.5c04144.

Morin, G., Ostergen, J.D., Juillot, F., Ildefonse, P., Calas, G., Brown, G.E., 1999. XAFS determination of the chemical form of lead in smelter-contaminated soils and mine tailings: importance of adsorption processes. Am. Mineral. 84, 420–434. https://doi.org/10.2138/am-1999-0327.

Mossop, K.F., Davidson, C.M., 2003. Comparison of original and modified BCR sequential extraction procedures for the fractionation of copper, iron, lead, manganese and zinc in soils and sediments. Anal. Chim. Acta 478, 111–118. https://doi.org/10.1016/S0003-2670(02)01485-X.

Nevidomskaya, D.G., Minkina, T.M., Soldatov, A.V., Bauer, T.V., Shuvaeva, V.A., Zubavichus, Y.V., Trigub, A.L., Mandzhieva, S.S., Dorovatovskii, P.V., Popov, Y.V., 2021. Speciation of Zn and Cu in Technosol and evaluation of a sequential extraction procedure using XAS, XRD and SEM–EDX analyses. Environ. Geochem. Health 43, 2301–2315. https://doi.org/10.1007/s10653-020-00693-1.

Noël, V., Boye, K., Kukkadapu, R.K., Bone, S., Pacheco, J.S.L., Cardarelli, E., Janot, N., Fendorf, S., Williams, K.H., Bargar, J.R., 2017. Understanding controls on redox processes in floodplain sediments of the Upper Colorado River Basin. Sci. Total Environ. 603, 663–675. https://doi.org/10.1016/j.scitotenv.2017.01.109.

Nordstrom, D.K., 2011. Hydrogeochemical processes governing the origin, transport and fate of major and trace elements from mine wastes and mineralized rock to surface waters. Appl. Geochem. 26, 1777–1791. https://doi.org/10.1016/j.apgeochem.2011.06.002.

Nriagu, J.O., 1974. Lead orthophosphates – IV. Formation and stability in teh environment. Geochim. Cosmochim. Acta 38, 887–898. https://doi.org/10.1016/0016-7037(74)90062-3.

Ohta, A., Kubota, R., 2016. Copper speciation in a collection of geochemical reference materials using sequential extraction and evaluation of the validity using XANES spectroscopy. Geostand. Geoanal. Res. 40, 117–134. https://doi.org/10.1111/j.1751-908X.2015.00335.x.

Owen, D.E., Otton, J.K., 1995. Mountain wetlands: efficient uranium filters – potential impacts. Ecol. Eng. 5, 77–93. https://doi.org/10.1016/0925-8574(95)00013-9.

Pérez-Moreno, S.M., Gázquez, M.J., Pérez-López, R., Bolivar, J.P., 2018. Validation of the BCR seuqential extraction procedure for natural radionuclides. Chemosphere 198, 397–408. https://doi.org/10.1016/j.chemosphere.2018.01.108.

Praharaj, T., Fortin, D., 2004. Determination of acid volatile sulfides and chromium reducible sulfides in Cu-Zn and Au mine tailings. Water Air Soil Pollut. 155, 35–50. https://doi.org/10.1023/B:WATE.0000026526.26339.c3.

Priadi, C., Le Pape, P., Morin, G., Ayrault, S., Maillot, F., Juillot, F., Hochreutener, R., Llorens, I., Testemale, D., Proux, O., Brown Jr., G.E., 2012. X-ray absorption fine structure evidence for amorphous Zinc Sulfide as a major Zinc species in suspended matter from the Seine River Downstream of Paris, Ile-de-France, France. Environ. Sci. Technol. 46, 3712–3720. https://doi.org/10.1021/es2041652.

Raksasataya, M., Langdon, A.G., Kim, N.D., 1996. Assessment of the extend of lead redistribution during sequential extraction by two different methods. Anal. Chim. Acta 332, 1–14. https://doi.org/10.1016/0003-2670(96)00227-9.

Ravel, B., Newville, M., 2005. ATHENA, ARTEMIS, HEPHAESTUS: data analysis for X-ray absorption spectroscopy using IFEFFIT. J. Synchrotron Radiat. 12, 537–541. https://doi.org/10.1107/S0909049505012719.

Regenspurg, S., Margot-Roquier, C., Harfouche, M., Froidevaux, P., Steinmann, P., Junier, P., Bernier-Latmani, R., 2010. Speciation of naturally-accumulated uranium in an organic-rich soil of an alpine region (Switzerland). Geochim. Cosmochim. Acta 74, 2082–2098. https://doi.org/10.1016/j.gca.2010.01.007.

Ruban, V., López-Sánchez, J.F., Pardo, P., Rauret, G., Muntau, H., Quevauviller, P., 2001. Harmonized protocol and certified reference material for the determination of extractable contents of phosphorus in freshwater sediments – a synthesis of recent works. Fresenius' J. Anal. Chem. 370, 224–228. https://doi.org/10.1007/s002160100753.

Rubio, B., Nombela, M.A., Vilas, F., 2000. Geochemistry of major and trace éléments in sediments of the Ria de Vigo (NW Spain); an assessment of metal pollution. Mar. Pollut. Bull. 40, 968–980. https://doi.org/10.1016/S0025-326X(00)00039-4.

Sakan, S., Dević, G., Relić, D., Anđelković, I., Sakan, N., Đorđević, D., 2015. Risk assessment of trace element contamination in river sediments in Serbia using pollution indices and statistical methods: a pilot study. Environ. Earth Sci. 73, 6625–6638. https://doi.org/10.1007/s12665-014-3886-1.

Sani, R.K., Peyton, B.M., Amonette, J.E., Geesey, G.G., 2004. Reduction of uranium(VI) under sulfate-reducing conditions in the presence of Fe(III)-(hydr)oxides1. Geochim. Cosmochim. Acta 68, 2639–2648. https://doi.org/10.1016/j.gca.2004.01.005.

Schöner, A., Noubactep, C., Büchel, G., Sauter, M., 2009. Geochemistry of natural wetlands in former uranium milling sites (eastern Germany) and implications for uranium retention. Geochemistry 69, 91–107. https://doi.org/10.1016/j.chemer.2007.12.003.

Seeber, J., Seeber, G.U.H., 2005. Effects of land-use changes on humus forms on alpine pastureland (Central Alps, Tyrol). Geoderma 124, 215–222. https://doi.org/10.1016/j.geoderma.2004.05.002.

Sekine, R., Marzouk, E., Khaksar, M., Scheckel, K., Stegemeier, J., Lowry, G., Donner, E., Lombi, E., 2017. Aging of dissolved copper and copper-based nanoparticles in five different soils: short-term kinetics vs. long-term fate. J. Environ. Qual. 46, 1198–1205. https://doi.org/10.2134/jeq2016.12.0485.

Sharma, N., Wang, Z., Catalano, J.G., Giammar, D.E., 2022. Dynamic responses of trace metal bioaccessibility to fluctuating redox conditions in wetland soils and stream sediments. ACS Earth Space Chem. 6, 1331–1344. https://doi.org/10.1021/acsearthspacechem.2c00031.

Sobolewski, A., 1999. A review of processes responsible for metal removal in wetlands treating contaminated mine drainage. Int. J. Phytoremediation 1, 19–51. https://doi.org/10.1080/15226519908500003.

Stetten, L., Mangeret, A., Brest, J., Seder-Colomina, M., Le Pape, P., Ikogou, M., Zeyen, N., Thouvenot, A., Julien, A., Alcalde, G., Reyss, J.-L., Bombled, B., Rabouille, C., Olivi, L., Proux, O., Cazala, C., Morin, G., 2018a. Geochemical control on the reduction of U(VI) to mononuclear U(IV) species in lacustrine sediments. Geochim. Cosmochim. Acta 222, 171–186. https://doi.org/10.1016/j.gca.2017.10.026.

Stetten, L., Blanchart, P., Mangeret, A., Lefebvre, P., Le Pape, P., Brest, J., Merrot, P., Julien, A., Proux, O., Webb, S.M., Bargar, J.R., Cazala, C., Morin, G., 2018b. Redox fluctuations and organic complexation govern uranium redistribution from U(IV)-

phosphate minerals in a mining-polluted wetland soil, Brittany, France. Environ. Sci. Technol. 52, 13099–13109. https://doi.org/10.1021/acs.est.8b03031.
Stetten, L., Lefebvre, P., Le Pape, P., Mangeret, A., Blanchart, P., Merrot, P., Brest, J., Julien, A., Bargar, J.R., Cazala, C., Morin, G., 2020. Experimental redox transformations of uranium phosphate minerals and mononuclear species in a contaminated wetland. J. Hazard. Mater. 384, 121362. https://doi.org/10.1016/j.gca.2022.10.018.
Steudel, R., 2020. The Chemical Sulfur Cycle. https://doi.org/10.2166/9781789060966_0011.
Syed, H., 2006. Comparison studies adsorption of thorium and uranium on pure clay minerals and local Malaysian soil sediments. J. Radioanal. Nucl. Chem. 241, 11–14. https://doi.org/10.1007/bf02347283.
Tessier, A., Campbell, P.G.C., Bisson, M., 1979. Sequential extraction procedure for the speciation of particulate trace metals. Anal. Chem. 51, 844–851. https://doi.org/10.1021/ac50043a017.
Ueshima, M., Hashimoto, Y., Sakanakura, H., 2019. Chemical stability of framboidal pyrite containing geogenic arsenic in alluvial sediments. J. Environ. Qual. 48, 1907–1912. https://doi.org/10.2134/jeq2019.04.0174.
Veeramani, H., Alessi, D.S., Suvorova, E.I., Lezama-Pacheco, J.S., Stubbs, J.E., Sharp, J.O., Dippon, U., Kappler, A., Bargar, J.R., Bernier-Latmani, R., 2011. Products of abiotic U(VI) reduction by biogenic magnetite and vivianite. Geochim. Cosmochim. Acta 75, 2512–2528. https://doi.org/10.1016/j.gca.2011.02.024.
Vega, F.A., Covelo, E.F., Andrade, M.L., 2006. Competitive sorption and desorption of heavy metals in mine soils: influence of mine soil characteristics. J. Colloid Interface Sci. 298, 582–592. https://doi.org/10.1016/j.jcis.2006.01.012.
Wang, Y., Frutschi, M., Suvorova, E., Phromavanh, V., Descostes, M., Osman, A.A.A., Geipel, G., Bernier-Latmani, R., 2013. Mobile uranium(IV)-bearing colloids in a mining-impacted wetland. Nat. Commun. 4, 2942. https://doi.org/10.1038/ncomms3942.
Wang, Y., Bagnoud, A., Suvorova, E., McGivney, E., Chesaux, L., Phrommavanh, V., Descostes, M., Bernier-Latmani, R., 2014. Geochemical control on uranium(IV) mobility in a mining-impacted wetland. Environ. Sci. Technol. 48, 10062–10070. https://doi.org/10.1021/es501556d.
Weber, F.A., Voegelin, A., Kretzchmar, R., 2009. Multi-metal contaminant dynamics in temporarily flooded soil under sulfate limitation. Geochim. Cosmochim. Acta 73, 5513–5527. https://doi.org/10.1016/j.gca.2009.06.011.
Wei, Y.L., Yang, Y.W., Lee, J.F., 2005. Lead speciation in 0.1 N HCl-extracted residue of analog of Pb-contaminated soil. J. Electron Spectrosc. Relat. Phenom. 144-147, 299–301. https://doi.org/10.1016/j.elspec.2005.01.218.
Yokoyama, T., Makishima, A., Nakamura, E., 1999. Evaluation of the coprecipitation of incompatible trace elements with fluoride during silicat rock dissolution by acid digestion. Chem. Geol. 157, 175–187. https://doi.org/10.1016/S0009-2541(98)00206-X.
Yu, Z., Liu, E., Lin, Q., Zhang, E., Yang, F., Wei, C., Shen, J., 2021. Comprehensive assessment of heavy metal pollution and ecological risk in lake sediment by combining total concentration and chemical partitioning. Environ. Pollut. 269, 116212. https://doi.org/10.1016/j.envpol.2020.116212.
Zhou, P., Gu, B., 2005. Extraction of oxidized and reduced forms of uranium from contaminated soils: effects of carbonate concentration and pH. Environ. Sci. Technol. 39, 4435–4440. https://doi.org/10.1021/es0483443.